EXPERIMENTAL CHARACTERIZATION OF THE EFFECT OF MICROSTRUCTURE ON DYNAMIC BEHAVIOR OF SiC

A Dissertation
Presented to
The Academic Faculty

By

Samuel R. Martin

In Partial Fulfillment
Of the Requirements for the Degree
Master of Science in Mechanical Engineering

Georgia Institute of Technology

June, 2004

EXPERIMENTAL CHARACTERIZATION OF THE EFFECT OF MICROSTRUCTURE ON DYNAMIC BEHAVIOR OF SiC

Approved by:

Dr. Min Zhou, Chair

Dr. Dattatraya Dandekar

Dr. Naresh Thadhani

Dr. Jianmin Qu

Date Approved: June 4th, 2004

To my parents, who always placed education at the top of the list.

ACKNOWLEDGEMENT

First I would like to thank my advisor, Min Zhou, for all his help and guidance. His energy made me more determined to explore every possibility. I would like to thank Datta Dandekar for his many consultations. Since the plate impact testing was conducted at ARL I found myself in his office the most and his contributions played a vital role to this study. I also would like to thank Naresh Thadhani and Jianmin Qu for their advice and suggestions.

I would like to mention my family and Donna for encouraging me and providing moral support throughout my research.

I would like to thank Jerry LaSalvia for obtaining the material samples and for his advice in the materials characterization. The help of Lou Ferranti, Greg Kennedy, and Matt McGill for getting me started with the material preparation at Georgia tech was appreciated. I would like to acknowledge the assistance of Matt Motyka who helped train me on the equipment for the materials characterization at ARL. I would also like to thank Tim Cline and Mike Blount for their assistance with the gas gun at ARL.

This research would not have been possible without the support of William Bruchey, former Acting Branch Chief of the Armor Mechanics Branch (AMB), for providing initial funding for the project and Mike Zoltoski, Branch Chief AMB, for continued funding.

TABLE OF CONTENTS

LIST OF TABLES

LIST OF FIGURES

LIST OF ABBREVIATIONS

ARL: Army Research Laboratory

SiC: Silicon Carbide

RH: Regular Hexoloy

EH: Enhanced Hexoloy

HEL: Hugoniot Elastic Limit

HIP: Hot Isostatic Press

VISAR: Velocity Interferometer System for Any Reflector

BIM: Beam Intensity Monitor

PMT: Photo Multiplier Tube

Al_2O_3: Alumina

AlN: Aluminum Nitride

B_4C: Boron Carbide

TiB_2: Titanium Diboride

FrS: French sintered SiC

FS&HP: French sintered and hot pressed SiC

K68: Kennametal Tungsten with Cobalt Binder

WC: Tungsten Carbide

SUMMARY

For roughly fifteen years the military has sought to use the properties of ceramics for armor applications. Current high-performance ceramics have extremely high compressive strengths and low densities. One ceramic that has been shown to be highly resistant under ballistic impact is silicon carbide (SiC). It has been found that even within the silicon carbides, those manufactured by certain methods and those with certain microstructural properties have advantages over others. In order to understand the microstructural reasons behind variations in ballistic properties, plate impact tests were conducted on two sintered silicon carbides with slightly different microstructures.

Two variations of a silicon carbide with the trade name Hexoloy SA were obtained through Saint Gobain. Regular Hexoloy (RH) and Enhanced Hexoloy (EH) are pressureless sintered products having exactly the same chemistries. EH went through additional powder processing prior to sintering, producing a final product with a slightly different morphology than RH. Samples of each were characterized microstructurally including morphology, density, elastic wavespeeds, microhardness, fracture toughness, and flexure strength. The characterization revealed differences in porosity distribution and flexure strength. It was determined that the porosity distribution in EH had fewer large pores leading to an 18% increase in flexural strength over that for RH.

The focus of the mechanics of materials community concerning dynamic material behavior is to pin down what exactly is happening microstructurally during ballistic events. Several studies have been conducted where material properties of one ceramic type are varied and the dynamic behavior is tested and analyzed. Usually, from one

variation to the next, several properties are different making it hard to isolate the effect of each. For this study, the only difference in the materials was porosity distribution.

Plate impact experiments were conducted at the Army Research Laboratory (ARL) using the gas gun facilities within the Impact Physics Branch. A VISAR was utilized to measure free surface velocities. Tests were performed on each material to determine the Hugoniot Elastic Limit (HEL) and spall strength. Spall strength was measured as a function of impact stress, and pulse duration. Results show very little difference in the HEL and spall strength of the RH and EH samples. Within the variability of the test results, the spall strengths were the same, independent of pulse width, and showed a trend similar to that found in other studies for SiC. The materials also demonstrated finite spall strength above the HEL. Finally, it was found that the HELs of the two materials were similar.

CHAPTER 1:

INTODUCTION AND LITERATURE REVIEW

Introduction

Ceramics are attractive for armor applications due to their high hardness and low density. For this reason, they have been the subjects of thorough in-depth ballistic testing both in the field and laboratory. Due to the extreme hardness values and compressive strengths, authors [1, 2] have recently documented a new mechanism in the defeat of long rod penetrators by ceramic armor packages. Instead of immediately penetrating the target, the penetrator material flows radially outwards in what has been termed “interface defeat”, which is the process of a long rod penetrator eroding and dwelling at the surface of a ceramic with minimal penetration. This mechanism is advantageous in that, not only does it defeat the projectile, but it also enables the armor to remain undamaged, allowing for multi-hit capabilities. Numerous ceramics have been studied in the literature, including: silicon carbide (SiC), alumina (Al_2O_3), aluminum nitride (AlN), boron carbide (B_4C), and titanium diboride (TiB_2). SiC has presented itself as one of the more attractive options due to its low density, good penetration behavior, and lower cost.

Lundberg et al.[2], performed a study that looked at the velocity range where interface defeat of a long rod penetrator transitions to more traditional penetration behavior. The velocity where this occurs is termed the transition velocity interval. A higher transition velocity correlates to increased resistance to penetration and greater

erosion of the projectile. Lundberg found SiC to have a higher transition velocity interval than TiB_2 and B_4C. Measurements of shock wave profiles have also shown that SiC and TiB_2 undergo deformation-induced hardening, which may give rise to improved ballistic properties [3]. B_4C shows the opposite: significant softening and loss of strength above the HEL [4]. Orphal et al. [5-7] later performed tests in which penetration depth versus impact velocity were examined. They found that under similar conditions, SiC demonstrated less penetration than B_4C and AlN.

In addition to experiments performed in the field, more controlled laboratory techniques have been utilized in an attempt to understand the mechanisms in which ceramics fail, and to correlate microstructural properties to ballistic performance. The reason is threefold. First, such data may offer insight to the materials scientist who can in turn design a better ceramic. Second, material modelers can incorporate the information into computer code used in simulating dynamic events. Finally, it may provide a cheaper technique for ceramists to evaluate their prototypes without more costly full scale testing. To more fully explain the latter, if a ceramic is known to fail ballistically by a certain mechanism, there may be a way to test for that same mechanism using a much cheaper and simpler static test. The interest of this study is to (i) quantitatively characterize two sintered silicon carbides with slightly different microstructures, (ii) study their response to dynamic loads, and (iii) develop a better fundamental understanding of microstructural influences on dynamic material behavior.

Planar plate impact experiments were used to characterize material behavior at high deformation rates and impact stresses. Typical strain rates were in excess of 10^5 and impact stresses ranged from 1-16 GPa. From free surface velocity profiles obtained

during experimentation, several dynamic, material properties were determined. The Hugoniot Elastic Limit (HEL) was taken to be the break in the slope between the elastic and plastic rise in the free surface velocity profile. Most authors agree that HEL is the ballistic measure of yield within the material under uniaxial strain. Spall strength is taken to be the measure of a material's dynamic tensile strength. Table 1, of Grady [3] gives a comprehensive set of values for HEL and spall for various ceramics. The values for a particular ceramic may vary depending upon processing and microstructure. Such influences are examined in this thesis.

Throughout the literature, it has been observed that even minute differences in microstructure drastically effect ceramic properties and ballistic performance. Variations in porosity, density, impurities, glassy phases, and grain morphology all influence performance. These microstructural entities are directly related to the processing techniques used to take the initial powders to the final product. The main methods are hot pressing, pressureless sintering, and reaction bonding. Silicon carbides of each of the three processing routes have been tested in the literature [8-11]. Each process uses different dopants to aid in sintering, remove glassy phases, isolate impurities, and assist in densification. This study will concentrate on the HEL and spall strengths of two sintered silicon carbides with different porosity distributions.

Literature Review

Effects of Microstructure on Dynamic Behavior of Ceramics

Inherently, ceramics will contain some cracks or flaws. These are introduced in the processing. Despite being held at sintering temperatures to allow time for

intergranular glass flow and stress equilization, post-sintering cooling from high temperatures leads to residual stresses due to thermal expansion mismatches. For larger grain sizes, these stresses may be large enough to cause spontaneous microcracking [12]. Residual stresses from thermal expansion mismatches also play a significant role when the ceramic is loaded, causing additional microcracks. Low fracture toughness of the ceramics and the length of these microcracks will determine spall strength and HEL [12, 13].

In addition to the microcracks, pores and impurities can be seen as flaws within the material. Quasi-statically it is the average flaw size that determines the strength in compression and the largest flaw size that determines failure strength in tension [13-15].

Effects on HEL

Bourne et al. [13], Raiser [12], and Longy and Cagnoux [14] performed studies on variations of alumina and found the HEL to decrease with increasing grain size. Raiser attributed smaller grain sizes to less residual stresses at triple junctions and grain boundaries, which increased the stresses needed to initialize intergranular flow, sliding, and microcracking. Bourne et al. noted that flaw size will scale with the grain dimension and thus the HEL should vary with the average grain size [13]. Similar trends in HEL can be found by looking at the data on B_4C in a study by Grady [16]. For example, the HEL was approximately 19 GPa and 17 GPa for B_4C materials with respective grain sizes of 3 microns and 10 microns. Glass content around grains was found to play no part in the HEL of alumina [12-14].

Longy and Cagnoux [14] found porosity to be the most important parameter determining the HEL. HEL decreased with an increase in porosity. In another study Longy and Cagnoux [17] used the star flyer technique of Kumar and Clifton [18] on alumina to show that grain plasticity began below the HEL and had the effect of closing pores. In pure, fine-grained alumina, this compaction was not accompanied by mircrocracking, even up to twice the HEL. The confinement imposed by this type of loading inhibited the activation of cracks. In the case of alumina with an intergranular glassy phase, the overall deformation was accompanied by a microcracking of the glass. However, microcracks were not interconnected up to twice the HEL. In a similar study by Cagnoux [19], he observed using spherical wave loading that plastic compaction was due principally to slips and no cracks were nucleated. It was also shown that in coarse-grained alumina, the plastic compaction was due principally to twins and cracks were twin-nucleated.

Longy and Cagnoux explained their findings in terms of microplasticity since they found no microcracks in the alumina samples above the HEL. The HEL represented a threshold from which the coupling between plastic deformation of grains and the macroscopic behavior of the sample became effective. Porosity had a modifying effect on the local stresses applied to each grain. Under similar loading conditions, higher porosity lead to higher local stresses applied to the grains. This effect lowered the plasticity threshold and hence, the HEL.

Bourne et al. [13] also demonstrated that increased porosity lowers the HEL in alumina. They explained the phenomena differently based on the assumption that local regions of microfracture around pore sites were caused by local release and pore collapse.

They suspect that HEL would be the condition where these damaged zones join, interact and lead to the eventual failure of the material.

Another study that showed the same trend in porosity and HEL was conducted by Brar, et. al. [20]. They showed HEL decreased linearly with increasing porosity in B_4C.

Effects on Spall Strength

Microfracture occurring in the bulk of the material during the compressive portion of loading is the cause of low spall strength observed in ceramics. The damaged zones become nucleation sites for fracture in tension. Bourne et al. [13] believe that the regions surrounding pores are partly responsible, due to local release and pore collapse leading to concentrated regions of damaged material. They found that spall strength increased with a decrease in porosity. The suspect that the lower strength glass/porous matrix fails more easily than the pure alumina grains, and the grain boundaries could be the favored routes which fractures might extend [13]. Raiser's work [12] on recovered alumina samples show this to be true.

While HEL was found to be more dependent upon grain size than glassy grain boundaries formed from impurities, Raiser [12] and Bourne et al. [13] found the exact opposite was true for spall strength. They found that with increasing glass content, spall strength decreases. It is interesting to note that glassy phases are less prevalent in hot pressed ceramics since fewer impurities are added to aid in sintering. Possibly the reason why hotpressed ceramics tend to have higher spall strengths as can be seen from the data by Dandekar [9] on SiC. In contrast, Longy and Cagnoux [14] noted little effect in their

work. They found porosity and grain size to affect spall with little correlation to glassy phase.

In some ceramics a trend in pulse length to spall strength has been observed. A longer pulse length correlates to a longer compressive portion of stress. If the compressive damage is time dependent, more damage will occur with an increased pulse width and the material will fail more easily in tension. Dandekar and Bartkowski observed this phenomenon in alumina [21]. Bourne [13] relates the time dependent process to the radius of damage around each pore. This radius is directly related to the crack velocity, which is in turn related to the sound velocity in the intergranular material.

Another reasonable assumption concerning spall strength is that a material with higher fracture toughness should have higher spall strength. A material more capable of resisting damage introduced during the compressive portion of loading would retain more strength upon experiencing tension and would demonstrate a higher spall strength.

Kennedy, et al. [22] performed a study that focused on the behavior of two-phase ceramics. They looked at TiB_2+Al_2O_3 ceramics with different phase (grain) sizes and connectivity. TiB_2 surrounded the alumina in one type and in the other it was considered interspersed, with the two uniformly intertwined. Results of HEL and compressive tests relied more on the average phase (grain) size. Spall strength scaled with TiB_2-phase interconnectivity. This result suggested that the interconnected TiB_2/Al_2O_3 morphology provided a stronger impediment to failure in tension. They attributed this difference to the possibility that the interconnected phase morphology was more effective in impeding initiation and progression of fracture under tensile conditions. Thus, TiB_2 likely had the ability to suppress and relax the cracks formed in alumina. In the two-phase

interdispersed structures, mechanical energy can become trapped due to scattering of waves from incoherent boundaries and interfaces, resulting in lower spall strength.

Despite being a different material, it is expected that SiC will follow similar trends in the relationship between microstructure and dynamic properties for the single-phase polycrystalline ceramics.

Dynamic Behavior of SiC

One of the first studies on silicon carbide was performed by Gust, et al. [23] roughly thirty years ago. In that study, shock waves in SiC induced by explosive-driven flyer plates were diagnosed by monitoring free-surface displacement using inclined-mirror streak-photography techniques. Since then many advancements have taken place in both materials processing of ceramics and experimental techniques for investigating dynamic phenomena.

HEL of SiC

Gust found a HEL of 8 GPa for his particular version of hot pressed SiC [23]. Grady and Kipp later did a report on a near theoretical density monolithic alpha SiC [24] made by Eagle Pitcher. The HEL was determined to be 15.3 GPa, which was approximately twice that of Gust. Grady attributed the increase to the substantially lower silica content from the SiC of the 1970s [4, 16]. Grady concluded that small variations in porosity had a large effect on HEL.

Grady [11] later performed a study on silicon carbide variations SiC-B, SiC-N, SiC-C, a reaction bonded SiC, and a microwave sintered version of the reaction bonded

SiC. All were produced by Cercom. SiC-B is a hot-pressed ceramic that used AlN as a sintering aid. SiC-N is similar to SiC-B but has an organic binder to get rid of the SiO_2 glass in the grain boundaries. Both had a nominal grain size of 4 microns. SiC-C followed the same process as SiC-N but had a smaller starting powder size of 1 micron. The subsequent grain size of SiC-C would be expected to be on the order of 1 micron, although this was not explicitly stated. The SiC-B and SiC-N had similar HEL values of 12 GPa and the SiC-C had a HEL of 13-14 GPa. From the data, it appears as if the organic binder did little to the HEL value, while the smaller grain size of SiC-C increased the HEL. The reaction bonded SiC was made by infiltrating a SiC and carbon preform with Si. The HEL for the reaction bonded SiC was similar to the Eagle Picher SiC of around 15-16GPa. The reaction bonded, microwave sintered material is just the reaction bonded SiC taken through an additional microwave sintering process. There was no difference between the two reaction bonded varieties. All the SiC ceramics showed significant hardening after reaching the HEL. The post yielding behavior is different between the Cercom hot pressed SiCs and reaction bonded variations. The SiC-B and SiC-C show significant post yield strength. The reaction bonded materials show behavior typical of pore collapse. The Cercom materials were also compared to the Eagle Pitcher material that was later found to have a grain size of 7 microns[11]. Despite having a bigger grain size, the HEL of the Eagle pitcher was higher than the SiC-C. However, when considering the post-HEL hardening as well, Grady concluded that the finest-grain, hot-pressed ceramic exhibited the highest dynamic strength of the ceramics, in this case SiC-C.

Bourne studied the shock behavior of a reaction bonded, hot pressed, and pressureless sintered SiC and also found that HEL and shear strength varied with processing route [8]. The reaction bonded HEL was 13.2 GPa with a density of 3.21 g/cm^3. The HEL of the sintered SiC was 13.5 GPa with a density of 3.16 g/cm^3. The hot pressed performed best, with an HEL of 15.7 GPa and a density of 3.23 g/cm^3. This data suggests that the HEL isn't necessarily a function of porosity, since the reaction bonded SiC is considerably more dense than the sintered but the HEL is approximately the same. This contradicts Grady's findings where the HEL of the reaction bonded ceramic was higher than his hot pressed variations.

In another study, Feng, Raiser, and Gupta obtained a SiC-B HEL of 11.5 GPa, with measured density of 3.214 g/cm^3 [10]. Their results match those of Grady for SiC-B. Feng, et al. found the strength of the material to be retained up to twice the HEL and they concluded that the shocked SiC did not have a distinctive elastic-inelastic transition at the HEL. They reasoned that the post-HEL evolution of the material strength resembled neither catastrophic failure due to massive crack propagation nor classical plasticity response. Qualitatively, they interpreted the response as a confinement-dependent inhomogeneous deformation involving both in-grain microplasticity and "percolation of highly confined microfissures."

Spall Strength in SiC

Bartkowski and Dandekar [25] conducted plane shock-wave spallation experiments on two silicon carbides. One material was SiC-B and the other was a sintered ceramic from Sohio. The materials were tested at impact pressures up to the

HEL of approximately 12 GPa. Their results indicated that the spall threshold of both silicon carbides increased with increasing impact stresses to 3.7 GPa, where spall strength peaked in both materials. The spall strength decreased with increasing impact stress after 3.7 GPa. The hot pressed ceramic had a peak threshold spall strength of 1.30 GPa and the sintered ceramic spall strength was 0.95 GPa around an impact stress of 3.7 GPa. The spall strength values of the hot pressed ceramic were higher than the sintered. The authors attributed this to better cohesion of the grains. The rise-fall behavior of the pre-HEL spall strengths was unique and suggested different, competing failure mechanisms. It was not clear whether the higher density or smaller grain size attributed to the greater spall strength in HP. The hot pressed ceramic was 99.3% pure and the sintered 98.2%. The density of HP was 3.22 g/cm^3 and sSiC was 3.16 g/cm^3. As was stated earlier in this chapter concerning alumina, it is interesting to note the lower purity of the sintered material.

Dandekar and Bartkowski [9, 26] performed spall strength tests on several additional US and French silicon carbides processed by hot pressing and sintering. They found the spall strength phenomena to be similar amongst all the varieties, independent of processing method. All materials initially increased in spall strength with increasing impact stress. Once a spall threshold was reached, it declined with increasing impact stress. The authors suggested that the relative dominance of plastic deformation over crack dynamics might have been the underlying reason for the observed increase in its spall strength with impact stress. The subsequent decline may have been due to the reversal of this dominance, where the crack dynamics dominated over plastic

deformation. The decline was attributed to generation and extension of microcracks under shock and release.

All the hot pressed materials showed higher spall strengths than the sintered materials. The Sohio sintered ceramic, due to its increased density, performed better than the French sintered (FrS). One of the materials studied, termed French sintered and hot pressed (FS&HP) was the French sintered material taken through an additional HIPing (hot isostatic pressing) step. This material showed unique characteristics. Although less experiments were conducted on this material than on its counterparts, it showed little scatter and a dramatic increasing trend in spall strength. FrS and FS&HP have the exact same chemistries. The HIPing dramatically reduced the porosity and increased spall performance. The measured densities for the two were 3.137g/cm^3 and 3.184 g/cm^3 for FrS and FS&HP, respectively. Beylat and Cottenot [27] determined the volume fraction percent of porosity of the two French varieties. FrS was 4.2% and FS&HP was 2.5%.

All the ceramics tested showed variability in spall strengths exceeding the precision of measurements. SiC-N showed significant scatter. This suggested that tensile strength was influenced by material variability. Such variability may be due to processing variation from batch to batch or a difference in the evolution of microcracks and/or defects. Regardless, there was a clear trend for a gradual increase then decline in spall strength with increasing impact stress.

Winkler and Stilp [28] did a similar study on a hot pressed SiC with a density of 3.19±0.02 g/cm^3. Their data showed that spall strength increased with increasing impact stress followed by a dip before the stated HEL of 13.0-14.7 GPa. After the HEL the spall strength remained at a low level. This pattern was similar to the French sintered and hot

pressed ceramic. The impact tests by Winkler and Stilp were conducted with varying pulse durations. Winkler also showed that SiC had higher spall strengths than TiB_2 and B_4C in the same study.

TiB_2 spall strengths stayed level until around 5GPa, and then subsequently decreased. Dandekar got similar results, with spall strength finally vanishing at the HEL of 13.5 GPa [29]. The B_4C spall strength remained constant. Dandekar [21] found Al_2O_3 maintains its original spall strength even at impact stress levels that exceed HEL.

Objectives

This thesis will study the microstructure of two variations of a sintered silicon carbide. The pore distribution of one leads to the material having a higher flexure strength. Chapter 2 will cover the material characterization, including fracture toughness and flexure strength. In addition to the material characterization, plate impact testing will be conducted to look at spall strength as a function of impact stress and pulse width along with HEL. Chapter 3 will explain the experimental setups and the theoretical background. Chapter 4 will present the results and the final chapter will be the conclusion.

CHAPTER 2

MICROSTRUCTURAL CHARACTERIZATION

Ceramic Processing Techniques

Due to its strong, covalent bonding and resulting high activation energy for self-diffusion, it was not believed that SiC could be pressureless sintered until 1973. Then Prochazka [30] discovered that with small additions of B and C these limitations could be overcome. It was a significant development, for it led to a low-cost route to a strong material. Today, Silicon carbide is used for abrasives, seals, refractory bricks, and increasingly, for armor applications. The different SiC processing techniques are described in detail in the book by Lee and Rainforth [31].

The mechanical properties of SiC are presumed to be dependent on the grain size of the powder, processing temperature, sintering aids, the powder blending process, and elemental composition of the compounds present in the processed materials. Silicon carbide cannot be consolidated without sintering aids. The conventional sintering aids for consolidation of SiC powder are boron, carbon, and aluminum nitride.

Complete understandings of the roles of each microstructural detail on the impact performance in SiC are not known; therefore a material characterization was performed on the samples to be tested. Optimally, just one variation in microstructure is desired in order to differentiate with certainty what impact it has on the material's overall dynamic behavior.

Regular Hexoloy and Enhanced Hexoloy

The materials used in this study go by the trade names Hexoloy SA and Enhanced Hexoloy and are commercially manufactured by Saint Gobain. In this thesis, the materials shall be abbreviated as RH for Regular Hexoloy and EH for Enhanced Hexoloy. The materials are both pressureless sintered silicon carbides of identical chemical composition. The only difference lies in their pore distributions. This is achieved by refining EH's presintered powder further with additional grinding and presintering compaction. The additional powder processing reduces the size of the largest flaw and therefore gives EH a higher flexure strength.

Material Properties

The sections to follow use standard techniques to characterize properties of RH and EH. Properties include density, elastic wave speeds, elastic constants, morphology, hardness, fracture toughness, and flexure strength. The elastic constants are calculated from the density and elastic wave speed measurements. Included in the morphology characterization are average grain size, grain aspect ratio, and pore size. Frequency percent distributions are formulated for all three with the latter also plotted as total frequency percent. Area fraction percent of pores and elongated grain coverage are calculated as well.

Density

Density measurements were conducted using Archimedes Principle, which determines density through water displacement. ASTM standard B311 titled "Density

Determination for Powder Metallurgy (P/M) Materials Containing Less Than Two Percent Porosity" gives a good summary of the technique used.

The test setup consisted of a glass container that rested on a stand straddling the weight pan of a precision balance (accuracy of 0.0001 gram). A wire frame with a hanger assembly was attached to the weight pan. The hanger assembly was such that a specimen could be weighed dry, and then could be weighed suspended in distilled water. Test specimens were cleaned of dirt, grease, and dust. They were also sufficiently smooth such that air bubbles would not adhere to any surface. The density of each sample was determined three times and averaged. The temperature of the water was also determined within 0.5 °C after each test, since the density of water varies with temperature.

The calculation for density is as follows:

$$\rho = \frac{m_{dry} * \rho_{H_2O}}{m_{dry} - m_{wet}} \tag{2.1}$$

where:

m_{dry} = dry mass of sample

m_{wet} = mass of sample submerged in water

ρ_{H2O} = density of water (varies with temperature)

Care must be taken when using density measurements for determining the amount of porosity in the material. Density measurements can be misleading if used when calculating percent porosity since other impurities are present in the material, such as sintering aids in sintered SiC. More dense sintering aids can lead to lower porosity calculations.

Three samples of each material were analyzed at Georgia Tech. Later 20 samples of each were analyzed at ARL. All the measurements were averaged and the density of RH was 3.152±0.006 g/cm^3 and EH was 3.156±0.005 g/cm^3.

Elastic Wave Speeds

Elastic wave speeds in the SiC were measured using non-destructive ultrasonic techniques. Glycerin was used as a couplant for the longitudinal wave speeds and honey was used for shear measurements. The transducer sent out a chirp signal and measured the successive reflections from the free surface of the sample. The travel time was averaged over three or four reflections. This time was used to determine the elastic longitudinal and shear wave speeds (see equations (2.2) and (2.3)).

Longitudinal wave speed:

$$c_l = \frac{2d}{t_l} \tag{2.2}$$

Shear wave speed:

$$c_s = \frac{2d}{t_s} \tag{2.3}$$

where:

d= thickness of specimen

t= elapsed time between a reflection (averaged over 3 or 4 reflections)

The reason for multiplying by two is that the wave travels to the free surface and reflects back to the transducer, traveling the thickness of the sample twice. RH had a longitudinal and shear wave speed of 12.03±0.04 km/s and 7.62±0.03 km/s, respectively.

The EH had a longitudinal and shear wave speed of 12.13±0.01 km/s and 7.64±0.02 km/s, respectively. The wave speeds were nearly identical and correlated well with results of other silicon carbides.

The bulk wave speed, although not directly measured, can be easily calculated using equation (2.4). The bulk wave speeds for RH and EH were calculated to be 8.21±0.08 km/s and 8.33±0.03 km/s, respectively.

Bulk wave speed:

$$c_o = \sqrt{c_L^2 - \frac{4}{3}c_s^2} \tag{2.4}$$

Calculation of Material Constants

Material constants were calculated from the measured densities and elastic wave speeds using theoretical derivations for wave propagation in solids found in Achenbach [32], also see ASTM Standard E494.

Longitudinal elastic impedance

$$Z_l = \rho * c_l \tag{2.5}$$

Young's modulus:

$$E = \left[\rho c_s^{\,2} \left(3c_l^{\,2} - 4c_s^{\,2} \right) \right] \Big/ \left(c_l^{\,2} - c_s^{\,2} \right) \tag{2.6}$$

Shear Modulus:

$$G = \rho * c_s^{\,2} \tag{2.7}$$

Bulk Modulus:

$$K = \rho\left[c_l^{\,2} - (4/3)c_s^{\,2}\right] \tag{2.8}$$

Poisson's Ratio:

$$\nu = \left[1 - 2\left(c_s/c_l\right)^2\right] \Big/ 2\left[1 - \left(c_s/c_l\right)^2\right] \tag{2.9}$$

Since the initial longitudinal wave speeds, shear wave speeds, and densities of RH and EH are similar, the elastic constants are similar as well. See Table 2.1 for values.

Microstructural Investigation

In order to investigate the grains it was necessary to section, polish, and etch the samples. All of these processes are described in detail in Appendix A. Samples were sectioned using a diamond saw and then polished. To ease polishing, the samples were mounted in Bakelite. These mounted specimens were placed in an automatic polisher capable of polishing six samples at a time. After polishing, the samples were removed from the plastic holder and etched in a modified-murakami solution to dissolve the grain boundaries. Pictures were taken at 500x on an optical microscope. For each material, orthogonal planes were analyzed to look for anisotropy. For each specimen, five different locations were sampled. The images were calibrated to scale according to magnification lens. The images were saved with the appropriate scale bar and analysis was later done using the software Image-Pro Plus. Figures 2.1 and 2.2 show the microstructures of RH and EH. No anisotropy was found.

Determination of Grain Size and Morphology

Average grain size, grain size distribution, average aspect ratio, and aspect ratio distribution were determined by converting the micrographs into black and white pictures using Adobe Photoshop. Once the binary images were produced (see Figure 2.3), they were inserted into Image-Pro Plus. The images were calibrated and the automatic counting function was used. The program automatically calculated values for grain area and aspect ratio. Grain area was calculated by counting pixels. The grain diameters were calculated from the grain area via the equation for a circle. The data from Image-Pro Plus was exported to excel were the results were averaged and then tabulated on a frequency percent basis. For RH, four micrographs from each of the orthogonal faces were analyzed. After talking with representatives from the company and taking the amount of time needed to enhance the images into consideration, only two micrographs of EH were analyzed. There was little difference in grain size distributions between the two materials as can be seen from Figure 2.4. Aspect ratio frequency percent distributions were obtained the same way. From Figure 2.5 it can be seen that there is little difference in the aspect ratio distribution as well.

When looking through the microscope at a lower magnification it was noticeable that EH had a larger number of elongated grains. This was not apparent from the grain size and aspect ratio distributions. Figure 2.6 and Figure 2.7 show micrographs of RH and EH, respectively at 100X magnification. The area fraction percent of elongated grains was calculated to give a more quantitative measure of the differences between the two materials. The areas of elongated grains over $1000\mu m^2$ and with an aspect ratio of at

least 8 were summed and divided by the total area of the micrograph to give area fraction percent. Ten micrographs of each material were analyzed. EH was found to have approximately 4% area fraction percent where RH had close to 0%. In following sections, it will be discussed what effect the elongated grains may have on material properties.

Determination of Pore Size Distribution and Pore Volume Percent

Un-etched micrographs were taken from polished samples of each material at x200 magnification. Figure 2.8 shows a micrograph of pores in RH and Figure 2.9 in EH. Since values were heavily dependent upon quality of polish, ten pictures were taken of the best-polished surface of each material. The same procedure used for grain sizes was used for the analysis of pores. The porosity distributions were found to differ, with RH having a higher number of large sized pores. RH had a slightly higher total area fraction percent of pores due to its slightly lower density. This calculation took the total area of pores and divided it with the total area of micrograph. RH demonstrated 3.50% and EH was 3.15%. Figure 2.10 shows pore size frequency percent distribution and Figure 2.11 shows total pore size frequency distribution. Each figure also has a "blow up" section on the right of the larger pore sizes since these are the critical flaws that more directly effect fracture strength. From the frequency distributions and the "blow up" section of the larger pores sizes, RH has the greater number of larger and smaller sized pores. The larger pore sizes, above 9 microns, are only seen in RH. While in proportion to the total number of pores analyzed the larger pores are small in number, the largest pores have a disproportionate and adverse effect on flexure strength. Cracks initiate from

these sites and due to the brittle nature of the material, propagate and cause the material to fail. An average of the maximum pore size was also calculated from ten micrographs of each material. For EH the maximum pore size was 7.39 microns while RH was 10.10 microns. Table 2.2 gives a summary of the values obtained.

Hardness

The diamond indenter used for hardness testing was a Vickers, meaning it was a square pyramid. ASTM Standard C1327 was followed for this testing. Each test was run for a duration of 20 seconds at 1kg load. Provided the cracks from the indentation edges were within the tolerable limits, the average of the two diagonals were measured and used in equation (2.10). Five valid tests were sampled from each orthogonal face of each specimen for a total of 15 tests per material.

Vickers Hardness in GPa:

$$HV = 0.0018544(P/d^2) \tag{2.10}$$

where:

P = load, N

d = average length of the two diagonals from indentation, mm

There was no difference in the values from each orthogonal face so they were all averaged for each material. The hardness values were 23.4±0.9 GPa and 23.3±1.6 GPa for RH and EH respectively.

Effect of Elongated Grains on Fracture Toughness

It was noticed that EH had a structure with elongated grains. Moberlychan, et al. [33] presented a SiC with improved fracture toughness which they attributed to elongated grains. The aspect ratios of some were in excess of 10. Termed ABC-SiC, since it used Al, B, and C as sintering aids, the microstructure consisted of elongated grains formed in a complex interlocking structure with a reported fracture toughness of 9.1 MPa$\sqrt{}$(m) and a four point bend strength of 650 MPa. These two values were attained using similar methods used in this thesis, which will be described shortly. The grain boundaries had an amorphous phase to enhance intergranular fracture. The elongated grains enhanced crack deflection and bridging, while the interlocking structure prevented grain pullout. They noted that all the higher toughness ceramics in the literature have elongated grains.

The paper further compared the ABC-SiC to Hexoloy SA (referred to as RH in this study). From microscopy, they found fracture surfaces of four point bend specimens to be transgranular for RH whereas for ABC-SiC it was intergranular with crack bridging regions behind the crack tip. Fractography of RH showed an overall smoothness similar to that of brittle glasses. Microcrack patterns from Vickers hardness indents show that the cracks in RH followed relatively straight paths, while the cracks in ABC-SiC exhibited deflections. The crack deflection and bridging caused the ABC-SiC material to have a higher fracture toughness value. The authors attributed the higher flexure strength to the higher fracture toughness.

Due to the elongated grain structure of EH, it was first believed that the material could have a higher fracture toughness value. Later tests and correspondence with the company revealed that this was not the case. The elongated grains were a by-product of

sintering conditions. In fact, in Lee and Rainforth [31], they note that elongated grains could be detrimental since they provide a larger flaw surface that lowers flexure strength. The elongated grains in EH were found to neither help nor hurt the material. Fracture strength was not adversely affected, nor was fracture toughness improved in EH.

Fracture Toughness

Fracture Toughness was completed using ASTM Standard 1421. Single Edge Precracked Beam (SEPB) specimens were used. Two Knoop indentations were placed across the center of the bottom face of the beams. The beams were loaded in such a manner that a sharp crack formed within a certain distance of the total height (defined as W in equation (2.11)) of the specimen as per the standards require. The samples were then loaded to failure under the half-B configuration of ASTM standard C1161 (see section on Flexure Strength). A load cell on the test frame recorded the failure load. This load, along with the average precrack length was entered into equation (2.11) to determine the fracture toughness.

Fracture toughness:

$$K_{Ipb} = \left[f\left(a/W\right)\right]\left[\frac{P_{\max}\left(S_o - S_i\right)10^{-6}}{tW^{3/2}}\right]\left[\frac{3\left(a/W\right)^{1/2}}{2\left[1-a/W\right]^{3/2}}\right] \qquad (2.11)$$

where:

$$f\left(a/W\right) = 1.9887 - 1.326\left(a/W\right) - \frac{\left[3.49 - 0.68\left(a/W\right) + 1.35\left(a/W\right)^2\right]\left(a/W\right)\left[1-\left(a/W\right)\right]}{\left[1+\left(a/W\right)\right]^2} \qquad (2.12)$$

where:

K_{Ipb} = fracture toughness

f(a/W) = function of the ratio a/W for four-point flexure

P_{max} = maximum load

S_o = outer span

S_i = inner span

t = thickness of specimen

W = top to bottom dimension of specimen

a = pre-crack crack length

The fracture toughness values were 2.62±0.05 MPa√m for RH and 2.54±0.05 MPa√m for EH. There is no noticeable difference and the value for RH matches that of Quinn [34]. The elongated grains in EH did not have the same effect on fracture toughness as the elongated grain structure of Moberleychan et al. [33].

Flexural Strength

Flexure strength was tested according to ASTM standard C1161. Type B, four-point bend specimens with loading at quarter points were used. Roughly 20 specimens of each material were loaded to failure. This failure load was entered into the beam equation for simply supported beams and the failure stress was calculated.

Flexural strength:

$$\sigma = \frac{3PL}{4wt^2} \tag{2.13}$$

where:

P = break load

L = outer support span

w = specimen width, and

t = specimen thickness.

The specimens were found to have differing flexure strength values, with the EH being stronger. Even though Lee and Rainforth [31] stated elongated grains may decrease the strength, this was not the case in EH. EH had a flexure strength of 450±40 MPa compared to RH's 380±30 MPa, correlating to an 18% increase.

Discussion

The materials are very similar in all properties. See Table 2.3 for a summary of values from the microstructural characterization. The values in parenthesis in Table 2.3 indicate how many samples were tested. Statistically, there is little difference in density, elastic wave speeds, and fracture toughness of the materials. There is a difference in the porosity distributions and also in flexure strength values. It is believed the latter two are directly related. In the subsequent chapters, it will be determined whether the differences play any part in dynamic behavior of the materials. It was interesting to note that such a small difference in pore morphology could correlate to the 18% increase in the flexure strength of EH.

There was also a small difference in area fraction percent of elongated grains. However, this was determined to have a no effect on the static properties of the materials.

Either there were not enough of the elongated grains or the grain boundaries were of comparable strength to the actual grains.

Table 2.1: Elastic Constants

		Regular	Enhanced
E	(GPa)	427±2	432±1
G	(GPa)	183±2	184±1
B	(GPa)	212±4	219±1
υ		0.165±0.007	0.171±0.003

Table 2.2: Microstructural Analysis Data

	Regular	**Enhanced**
Avg. grain size (μm)	3.47	3.79
Avg. aspect ratio (μm)	2.05	2.00
Elongated grain area frac. %	4%	0%
Average pore size (μm)	2.65	2.74
Pore area frac. %	3.50%	3.19%
Avg. max pore size (μm)	10.10	7.39

Table 2.3: Summary of Material Properties

		Regular	Enhanced
density	(g/cm^3)	3.152±0.006	3.156±0.005
C longitudinal	(km/s)	12.03±0.04	12.13±0.01
C shear	(km/s)	7.62±0.03	7.64±0.02
C bulk	(km/s)	8.21±0.08	8.33±0.03
Fracture Strength (4pt-bend)	MPa	380±30 (25)	450±40 (22)
Fracture Toughness (SEPB)	MPa√(m)	2.61±0.05 (5)	2.53±0.05 (5)
Vickers Hardness (1 kg, 20 s)	(GPa)	23.4±0.9 (9)	23.3±1.6 (10)
Avg. grain size	(μm)	3.44	3.79
Pore area fraction %		3.50%	3.19%
Elongated grain area fract. %		4%	~0%
Size of largest pore	(μm)	10.10	7.39

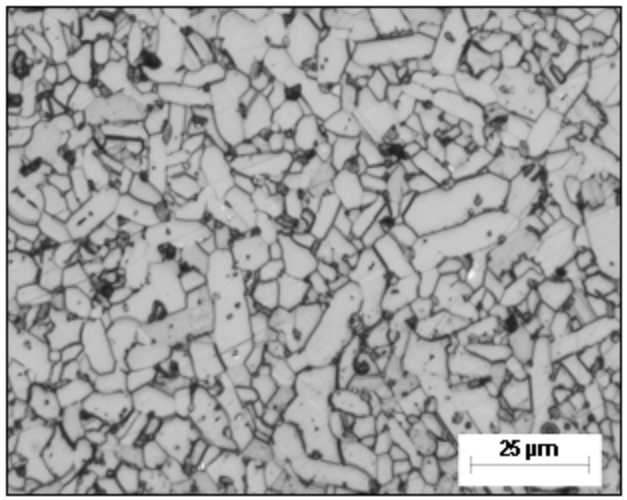

Figure 2.1: Regular Hexoloy X500

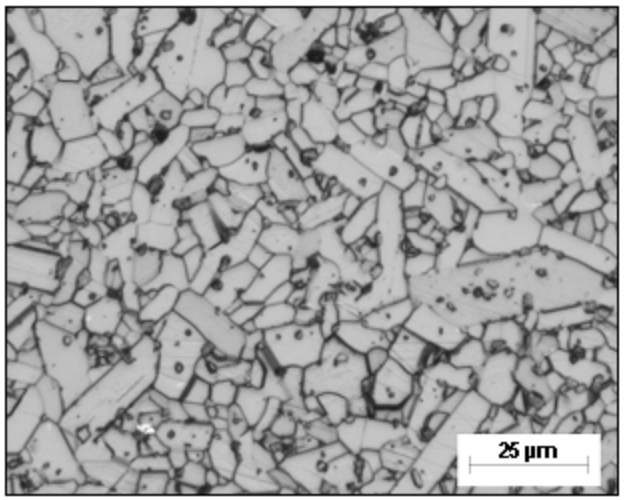

Figure 2.2: Enhanced Hexoloy X500

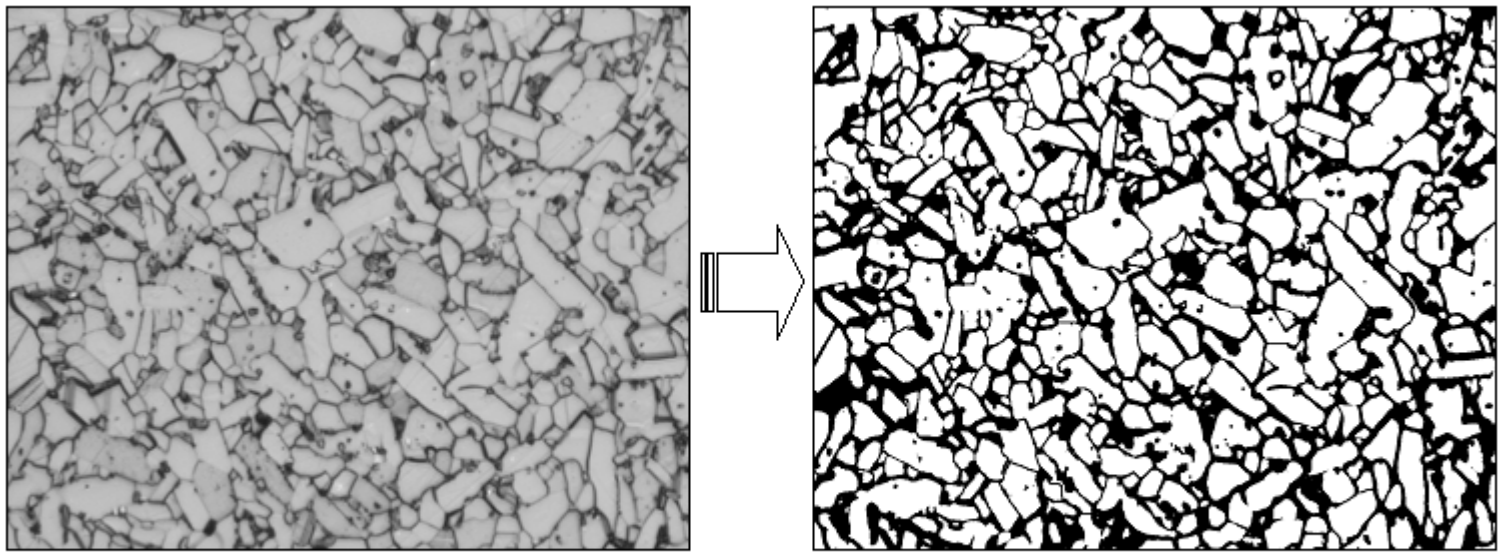

Figure 2.3: Grayscale to Binary (black/white) Image

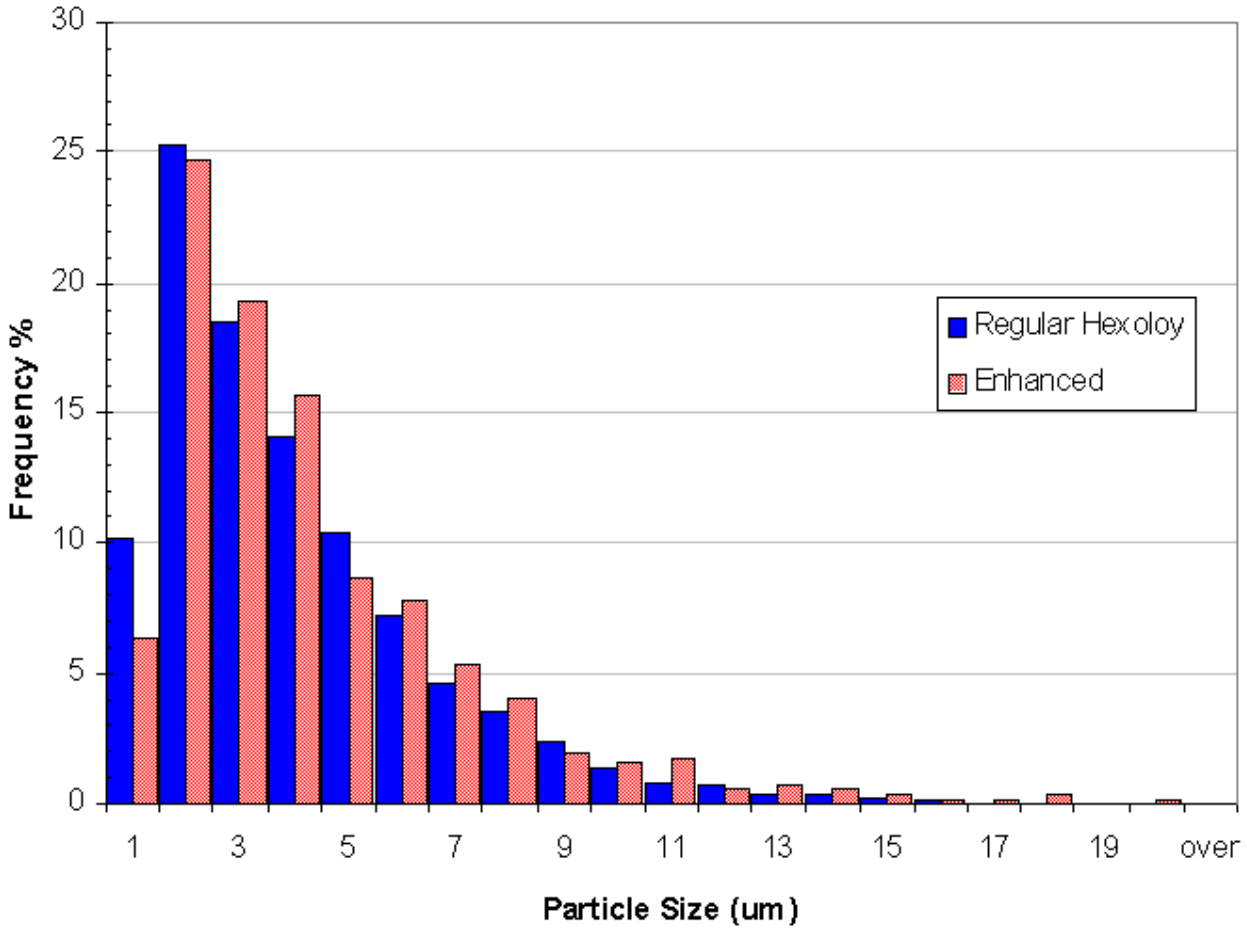

Figure 2.4: Grain Size Frequency % Distribution

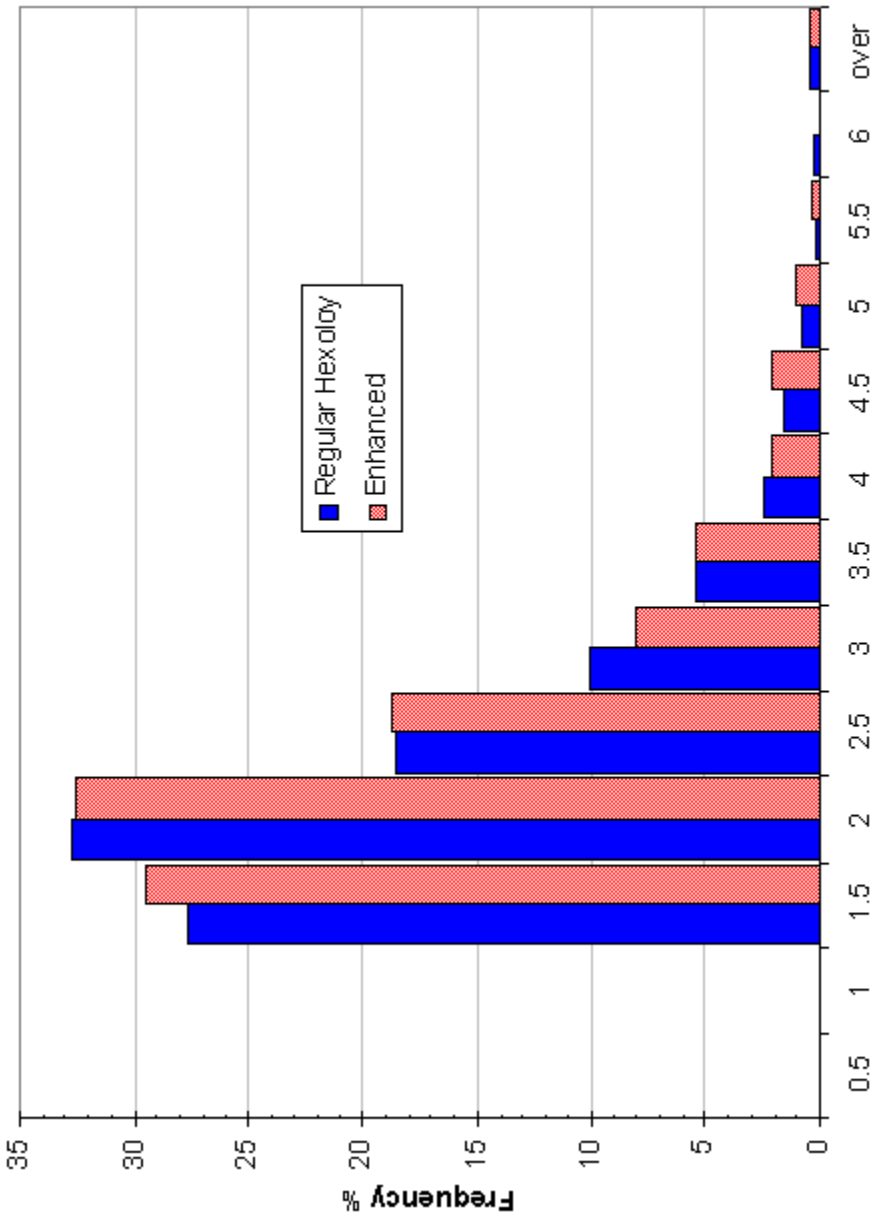

Figure 2.5: Aspect Ratio Frequency % Distribution

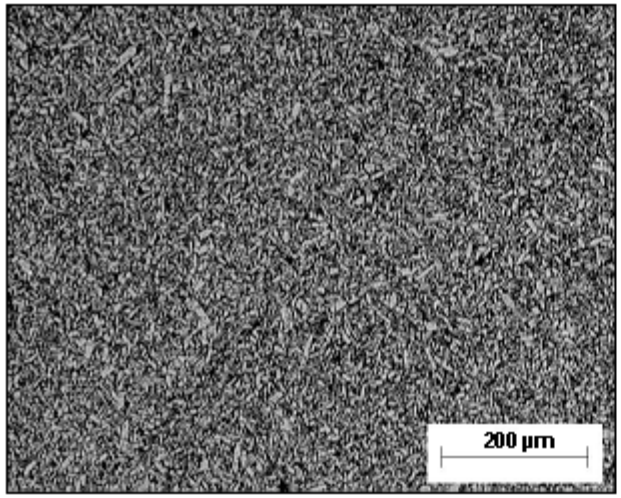

Figure 2.6: Regular Hexoloy X100

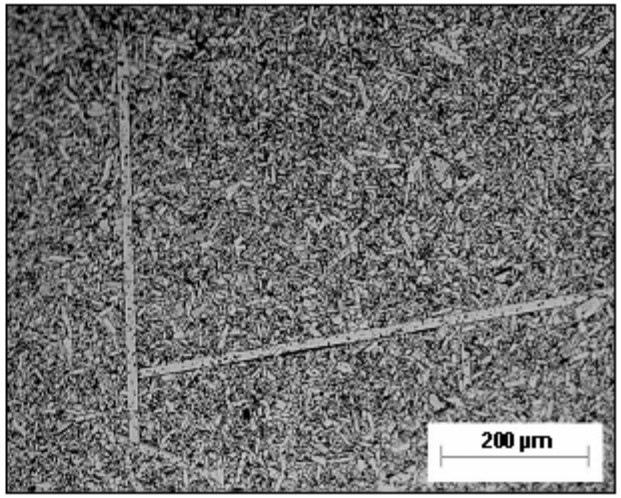

Figure 2.7: Enhanced Hexoloy X100

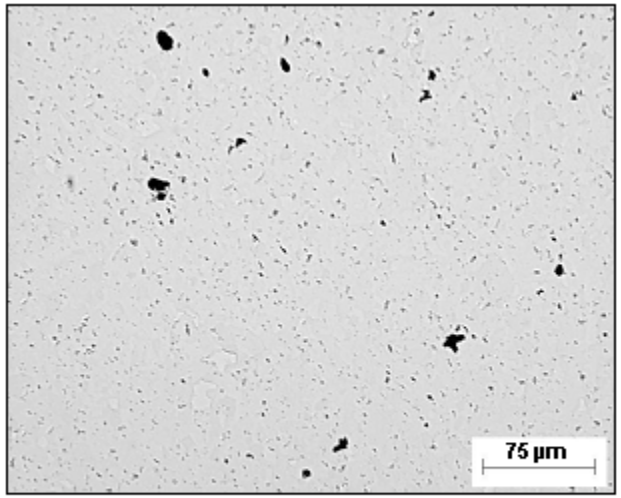

Figure 2.8: Regular Hexoloy X200

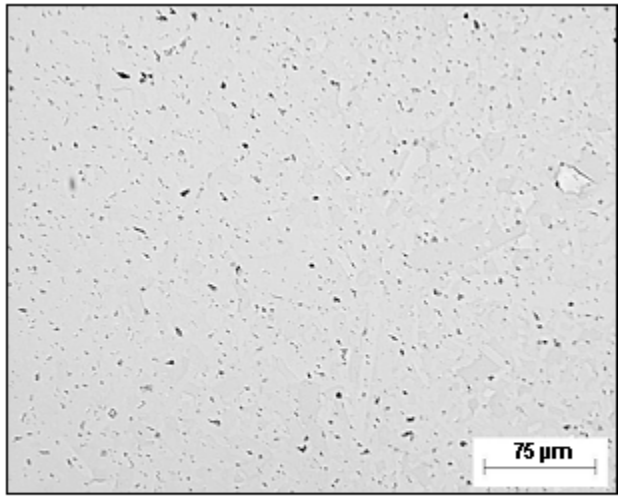

Figure 2.9: Enhanced Hexoloy X200

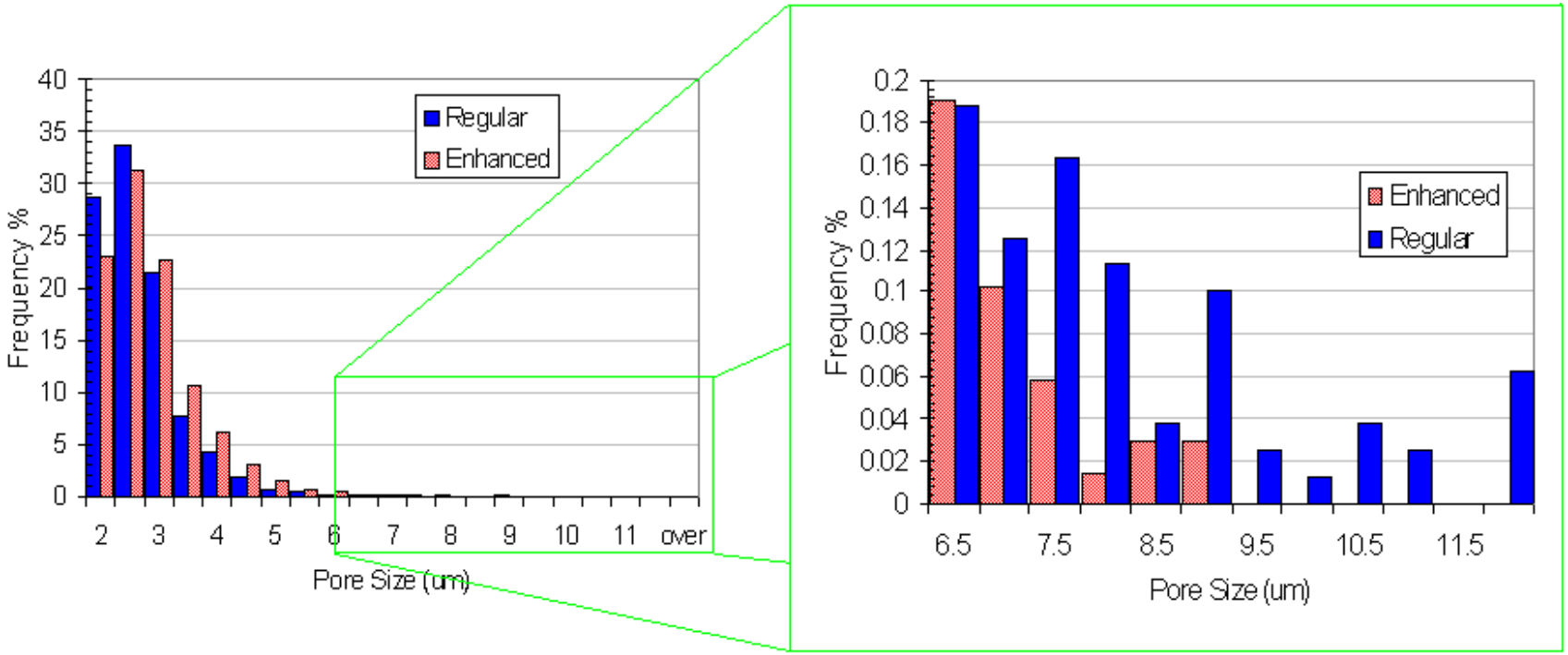

Figure 2.10: Pore Size Frequency % Distribution w/ Blowup of Larger Pore Sizes

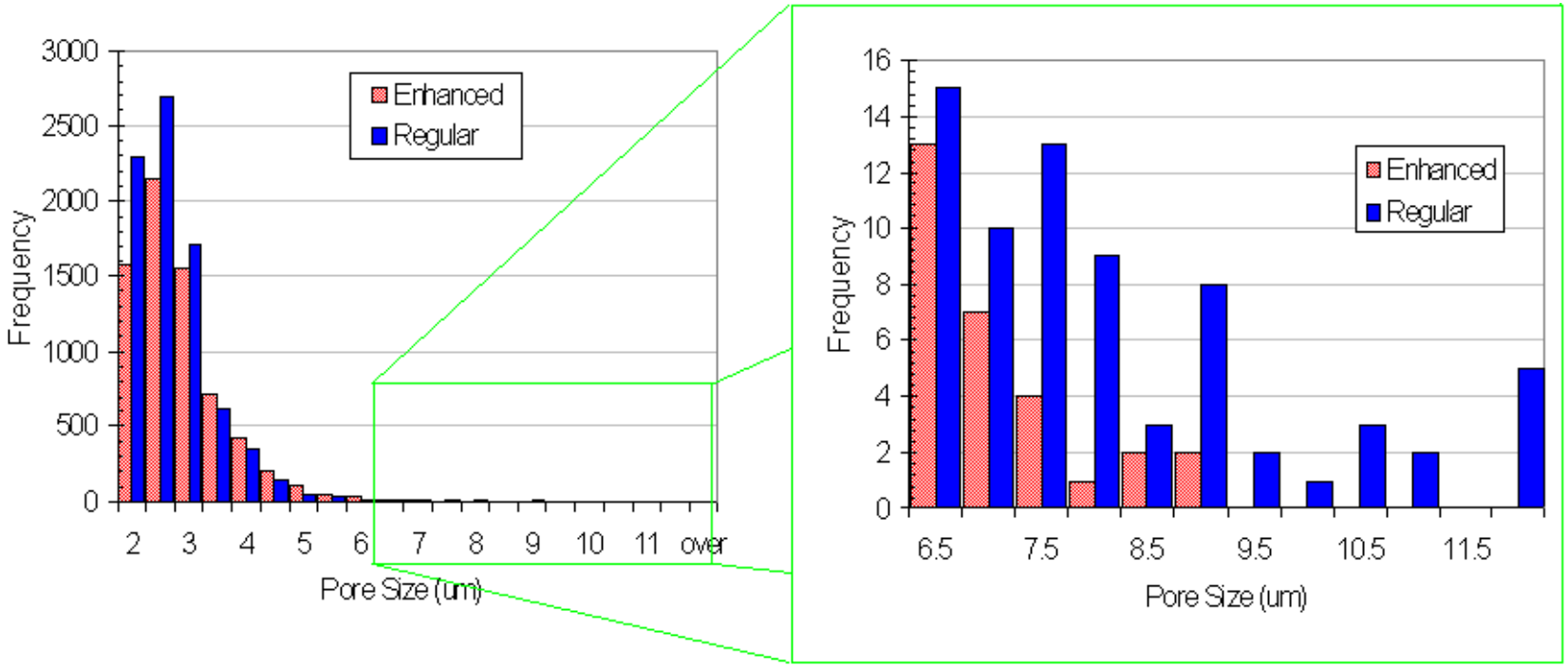

Figure 2.11: Pore Size Total Frequency Distribution w/ Blowup of Larger Pore Sizes

CHAPTER 3

EXPERIMENTAL CONFIGURATIONS

Plate Impact Experiment

Plate impact testing was conducted at the Army Research Laboratory using the gas gun facility in the Impact Physics Branch. The gas gun has a 102 mm bore diameter and is 8 meters long. The gun consists of a breech, barrel, target chamber, and catch tank, see Figure 3.1. Velocities from 80-700 m/sec can be achieved and four VISARs are available for free surface velocity measurements. The barrel had a keyway that allows side-by-side experiments to be conducted.

Data was collected using push-pull VISARs with the probes focused at the back surface of the specimen. Oscilliscopes collected the projectile velocity measurements and VISAR signals. A labview program interface was used for operating the gun and a seperate data reduction program was used to analyze the VISAR data. The reduction program converted interference fringes to free surface velocities.

VISAR

VISAR is the acronym for Velocity Interferometer System for Any Reflector developed by Barker and Hollenbach in 1972 at Sandia National Laboratory [35]. The system works off the principle of Doppler shift. A laser beam is separated into a reference and delay leg. Particle velocity at a free surface can be obtained from the

interference fringes created between the two legs as a result of the movement of the reflective surface.

The system consists of a laser, a probe, a VISAR interferometer, oscilloscopes, and the necessary optic couplings and wiring. The laser beam is optically coupled to a fiber that runs into a splice box. The probe inlet is spliced to this. The probe is placed 30 mm from the reflective rear surface of the target. "Reflective" is a relative term with the optimum being between specular (mirror-like) and diffuse. The laser beam reflected from the back of the target is collected in the same probe. The beam travels back to the splice box where the output line is connected to the VISAR optical fiber, see Figure 3.2.

Once in the interferometer, the beam is divided into a Beam Intensity Monitor (BIM) and a beam that is later separated again, see Figure 3.3. The BIM is used for diagnostic purposes. The other beam is split into the reference leg and the delay leg. The delay is achieved by placing precisely calibrated glass etalons in one path of the split laser beam. The object of the delay is to achieve a 90-degree phase difference between the two beams. The beams are converted into electrical signals via photo multiplier tubes (PMT), which are connected to oscilloscopes.

When the surface is moved the reference and delay beams produce light fringes. The fringes can be correlated to free surface velocity since the etalons have been calibrated. Final particle velocities have an accuracy of 1%.

Plate Impact Specimens

Plate impact specimens were machined to strict tolerances for spall tests. Cylindrical specimens were machined with thicknesses of 2.047±0.003 mm, 4.047±0.003

mm, and 6.397±0.003 mm. Each face was flat to within 3 light bands, parallel to within 5 microns of the opposite face, and polished to a mirror finish. All specimens were 31.8±0.03 mm in diameter.

Experimental Setup

The flyer was set in a flyer ring using epoxy. The flyer was backed with a foam plug to assure a traction-free back surface while adding stiffness. For higher velocities an additional aluminum strap was placed on the back of the flyer ring for extra rigidity. Once the epoxy was cured, the flyer ring with flyer was epoxied onto the front end of an aluminum projectile, see Figure 3.4. The target was assembled in a similar manner; with the target set into the target ring using epoxy. Brass contacts were also epoxied into the assembly that would serve to trigger data collection, see Figure 3.4. Figure 3.5 shows a front view of the flyer and Figure 3.6 shows a front view of the target. The flyer also has a small hole drilled into the epoxy, which is not shown in Figure 3.5, so the inner chamber of the projectile could be evacuated when a vacuum was pulled. When cured, the target assembly was attached to an adjustable mount in the target chamber at the end of the barrel. During setup the mount was adjusted such that the target was perfectly planar to the flyer. This was accomplished using laser alignment techniques.

To measure velocities a set of four pairs of pins were arranged directly in front of the target such that when the projectile passed, the pins shorted. An oscilloscope recorded when the pins shorted allowing velocities to be calculated. Distances between pins were accurately measured beforehand. The velocity readings from the pins were averaged to obtain the striking velocity.

For the shot, the target chamber was sealed with the probe focused on the back of the target. The catch tank was attached to the target chamber to stop the projectile and collect all the debris from the shot. A diaphragm was placed between the two chambers before each was placed under vacuum separately. The diaphragm makes the process of evacuating all the air more efficient as the two volumes of the target chamber and catch tank are much different. The chambers were then placed under vacuum to alleviate the system from the high-pressure air that would accumulate in front of the projectile otherwise.

For the shot, the projectile was placed under vacuum at the breech end of the gun. Meanwhile, the breech chamber was pressurized. When the gun was "fired" the vacuum behind the projectile was released allowing it to be initially sucked down the tube. Once the end of the projectile passed the radial openings to the high-pressure air of the breech, the projectile attained full momentum.

Theory

For a plate impact test, it is desirable to have one-dimensional wave propagation to simplify analysis of material behavior. This can be achieved by making the diameter of the specimen much larger than the length. If the VISAR probe is centered on the back surface of the target, then the initial data from the experiment should be completely one-dimensional effects.

Assuming linear elastic properties in the material below the HEL, the one-dimensional waves can be tracked using the longitudinal elastic wave speed measured from ultrasonic testing. A time versus position (x-t) plot is useful to study wave

interactions and can aid in the design of experiments. Varying the thickness of the flyer controls the duration of the compressive pulse and adjusts the location of the spall plane. From the x-t diagram and initial conditions, a stress versus particle velocity (σ-u) plot can be developed to determine the stress values achieved in the flyer and target throughout impact. The states in the material are found using the characteristic equations $\sigma \pm Z * u = const.$ along $dx/dt = \pm c_L$. The states of stress and particle velocity in adjacent regions are connected along straight lines of slope ±Z. Thus varying the impact velocity gives direct control of the magnitude of stress. Stress states in the materials can also be changed depending on the impedance value of the flyer. Plate impact experiments were designed using these tools and is described in more detail below.

Spall Strength

Spall strength is defined as the amount of strength a material retains upon first experiencing tension. At impact, a shock induced compressive wave moves through the material. Upon reaching the free surface of the target, the wave reflects as a tensile wave. Where this wave reacts with the end of the compression wave is where the target first experiences tension. If the stress is above the spall threshold, cracks will initiate and coalesce along a spall plane. The spall plane creates a free surface and causes additional reflections. Wave reflections can be observed by the VISAR at the free surface of the target.

Spall strength can vary with impact stress and duration of compressive pulse. The former is believed to be a result of the magnitude of compressive damage; the latter

provides information on the time-dependent damage experienced by the material throughout the initial compressive wave.

When impacted, if the stress does not exceed the spall threshold value, then the free surface velocity will return to zero indicating there was no spallation. If the stress is high enough to induce spallation, then a drop in velocity will occur. Shortly thereafter the velocity will rise again indicating the stress wave has reflected off the newly created surface within the target. The magnitude of this drop from the initial Hugoniot stress state indicates the spall strength. If the velocity profile never decreases there is no spall strength in the material.

Identification of Spallation on an X-T Diagram

The x-axis of an x-t diagram indicates position with zero defined as the interface between the flyer and target. The y-axis indicates time with zero defined as the moment the flyer impacts the target. Upon impact, compression waves propagate into both the flyer and target at their respective longitudinal elastic wavespeeds. This is represented on the x-t diagram by drawing lines with slope $1/c_L$ back into the flyer and into the target; see Figure 3.7 and Figure 3.8. Figure 3.7 is the x-t diagram of EH with a 2mm flyer and Figure 3.8 is EH with a 4mm flyer. All lines within the flyer should be of slope $1/c_L$ of the flyer, and all lines within the target should be of slope $1/c_L$ of the target. The compressive waves reflect off the free surfaces and travel back into the materials as tensile waves. The tensile wave in the target is called a release wave. For a symmetric impact, where both the flyer and target are the same material, the tensile wave from the flyer represents the end of the compressive pulse. The time (y-value) where this wave

hits x=0 is considered the pulse width, denoted pw in Figure 3.7 and Figure 3.8. Pulse width can also be calculated using equation (3.1). The line representing the end of the compressive pulse is extended into the target. Where this line intersects the release wave within the target indicates the position and time the material will first experience tension. Spallation will occur at this time and location. For a symmetric impact, spallation within the target will occur exactly one flyer thickness from the free surface.

Pulse width:

$$pw = 2 * \frac{th_{flyer}}{c_{L\_flyer}} \tag{3.1}$$

where:

pw= pulse width

th_{flyer}=thickness of flyer

c_{L_flyer}=longitudinal wave speed of flyer

Estimate of Spall Strength from Free Surface Velocity Profile

A graphical method was employed to calculate spall strength. Knowing the impedance of the flyer and target and also knowing the impact velocity, a σ-u graph such as Figure 3.9 was formulated. The target material starts at velocity 0 and the flyer begins at the striking velocity. Both materials experience no stress before impact. Upon impact, the stress state achieved is the intersection of the lines formed by the impedances. The state in the material at this point is termed the hugoniot state. The target starts at (0,0) and moves to the right with a slope of its impedance. The flyer moves from ($V_{striking}$,0) backwards at a slope of minus its impedance. The y-value of this intersection indicates

the impact stress. The x-value of the intersection is the particle velocity at impact. For symmetric impact this value is half of the impact velocity. The target moves to the right from this intersection at a slope of minus its impedance. The target will unload and the stress will be zero, however, the particle velocity will not be zero. The particle velocity can be measured at the free surface of the target using the VISAR. For a symmetric impact the free surface velocity should be the same as the hugoniot velocity measured by the VISAR. The change in velocity from the hugoniot state to the dip in the VISAR free surface velocity profile is used to calculate the spall stress. This change in velocity is called pullback and can be seen in Figure 3.10. On the σ-u diagram, pullback is subtracted from the particle velocity of the target and two lines of slope of ± the target impedance are drawn underneath in the minus y region, indicating tension. The y-value of this intersection is the spall strength of the material at that impact velocity. Spall strength can also be calculated using equation (3.2).

Spall:

$$\sigma_{spall} = \frac{1}{2}\Delta v * Z_{tar} \tag{3.2}$$

where:

Δv=pullback

Z_{tar}=elastic impedance of target

Experimental Configuration for Determining Spall Strength

All spall tests at impact stresses below the HEL were symmetric, with flyer and target of the same material. Tests were completed with flyers of nominal thickness 2mm and 4mm. This was done to achieve two different pulse widths to test for time-

dependence of damage within the samples. Targets were 6.4 mm thick. See Figure 3.7 and Figure 3.8 to see how pulse width changes with flyer thickness. All SiC samples were 31.8 mm in diameter. This l/d ratio was so that cylindrical release waves would not interfere with the measurement of the longitudinal waves. The time before arrival of the cylindrical wave is calculated as follows:

$$t_{cylindrical} = \frac{\sqrt{th_{tar}{}^2 + \left(d_{\min}/2\right)^2}}{c_{L\_tar}} \tag{3.3}$$

where:

$t_{cylindrical}$ = time when cylindrical wave arrives

th_{tar} = thickness of target

d_{min} = the lower of the diameters between the flyer and target

c_{L_tar} = longitudinal wave speed of the target

The diameters were also such that two samples could be fired side by side in one shot. For side-by-side shots, two probes and two VISARs were used, one for each sample. Testing this way had the increased benefit of allowing two tests to be run at exactly the same conditions (i.e. identical striking velocity).

Specimens were placed side by side on most shots. For one shot EH and RH, each with identical flyer thicknesses, were tested simultaneously. The majority of the other side-by-side shots were conducted using the same material but with different pulse widths. Side by side testing required a key to be placed on the projectile to prevent spinning of the projectile during the shot. A key was used for single shots as well.

Experimental Configuration for Determining Spall Strength Above HEL

Due to the limitations of the gas gun, in order to achieve an impact stress above the HEL it was necessary to switch the flyer to a higher impedance material. A symmetric impact would require a velocity beyond the pressure ranges of the gun. The higher impedance material forces the impact stress to increase see Figure 3.11. The calculation for impact stress above the HEL is slightly different from the process described earlier.

The impedance of the material changes upon reaching the HEL to the plastic impedance, which is merely the bulk sound speed multiplied by the density. This can be represented graphically on a σ-u diagram by having the target go from (0,0) at a slope of Z_{el} to the HEL. At this point the slope becomes Z_{pl}. In all likelihood the HEL of the projectile will be exceeded as well. The same technique is employed with Z_{el} and Z_{pl} of the flyer. The intersection of the plastic impedances of the target and flyer give an estimate of the impact stress achieved. The target will unload elastically and the slope is simply $-Z_{el}$. Figure 3.12 gives an example of such an analysis.

K68 was used as the higher impedance material in shots 0405H* and 0408H*. K68 is a tungsten alloy with cobalt binder produced by Kennametal. For K68, the above assumption for calculating impact stress was invalid. Instead, the hugoniot curve was known, and instead of the Z_{el} and Z_{pl} slopes, the actual curve was placed in the stress versus particle velocity graph. The intersection of the hugoniot curve and Z_{pl} of the target gave a reasonable prediction of the impact stress. Figure 3.12 shows an analysis of shot 0405H*. A simple check is to compare the predicted target particle velocity in the

released state from the σ-u diagram with the measured hugoniot state free surface velocity measured from the VISAR.

HEL

According to Grady [16] the HEL "identifies the axial stress at which a solid, loaded in compression under constraint of uniaxial strain, can no longer support elastic distortion and begins to flow through plastic or cataclastic (crushing) fracture processes." Bourne et al states, "most authors agree that the HEL for a ceramic provides a threshold below which the material retains some cohesion and has finite spall strength and above which the material has zero spall strength and becomes an inertially confined powder."[13]

HEL can be seen on free surface velocity graphs and is represented by a slope change on the rise to the hugoniot state. The free surface velocity at the break in elastic rise is used to calculate the HEL. Equation (3.4) calculates HEL.

$$HEL = \frac{v * Z_{el}}{2} \tag{3.4}$$

Originally, HEL experiments were attempted with 6.4mm thick targets. However, the transition from elastic to plastic was not very pronounced. Therefore thicker target specimens were prepared to exaggerate this effect and make the transition more visible. Tungsten Carbide (WC) from Cercom was used with 9.9 mm thick SiC targets. The elastic-plastic responses of WC and SiC were adequate to calculate impact stress (Figure 3.12).

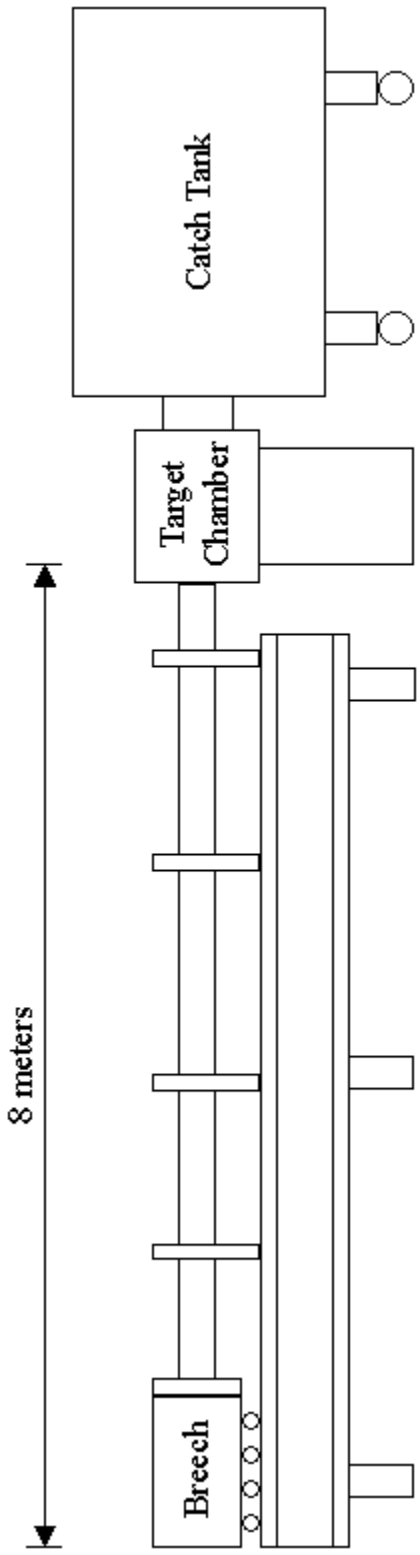

Figure 3.1: Gas Gun Schematic

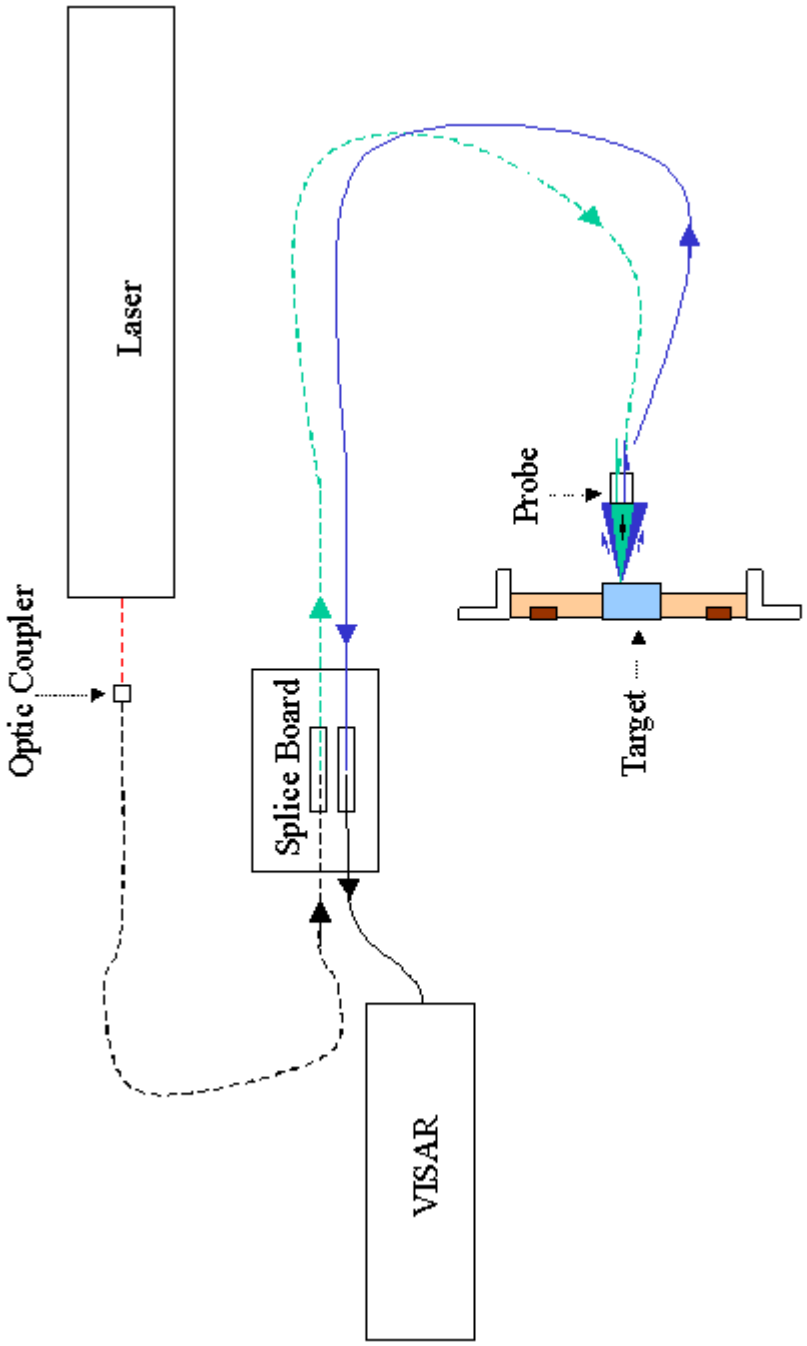

Figure 3.2: Probe Setup

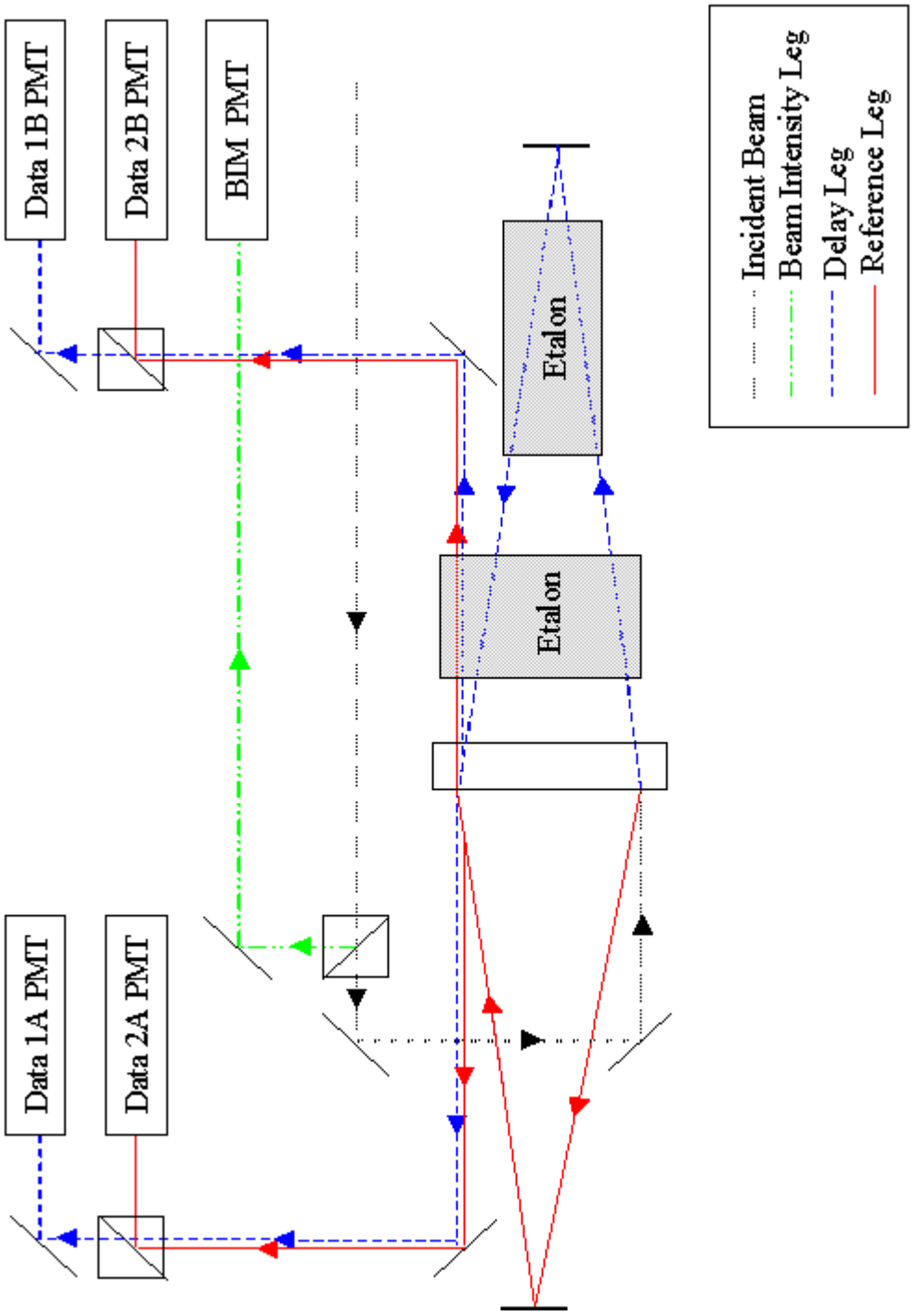

Figure 3.3: VISAR Configuration

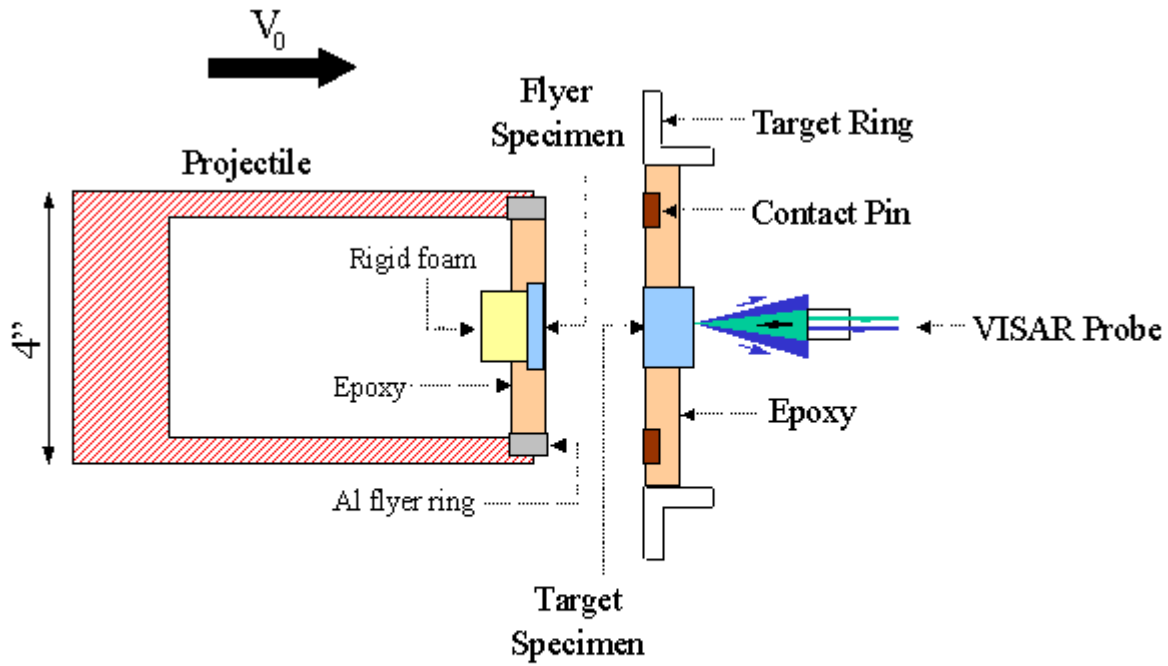

Figure 3.4: Diagram of Cross Section of Projectile and Target

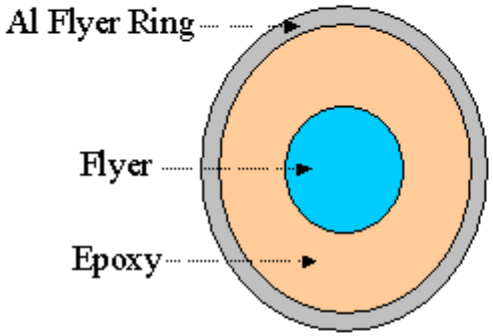

Figure 3.5: Front View of Flyer

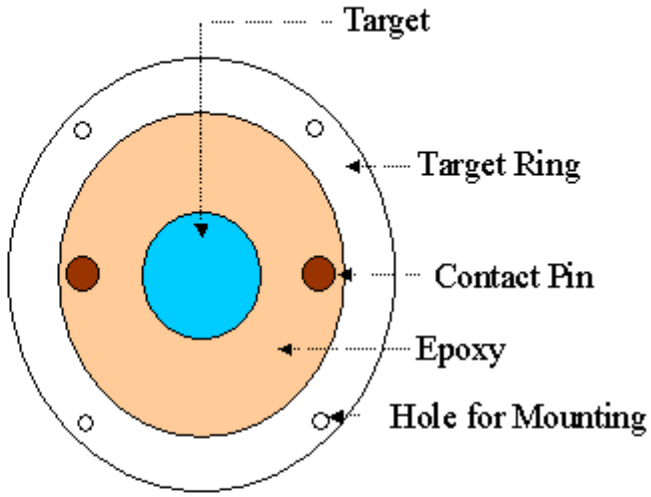

Figure 3.6: Front View of Target

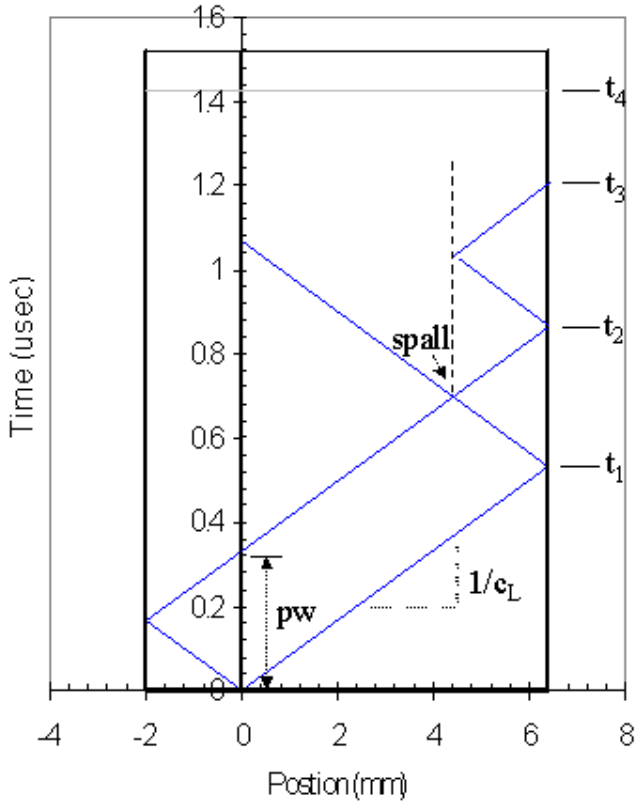

pw=pulse width
t_1=compressive pulse reading in VISAR
t_2=spall reading in VISAR
t_3=additional reflection off spall surface
t_4=arrival of cylindrical release

Figure 3.7: X-T Diagram 2mm Flyer

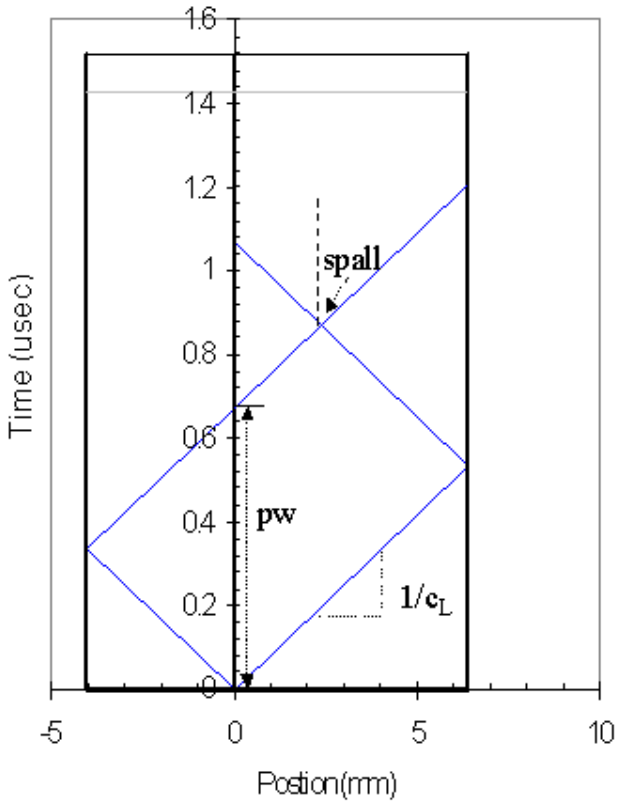

Figure 3.8: X-T Diagram 4mm Flyer

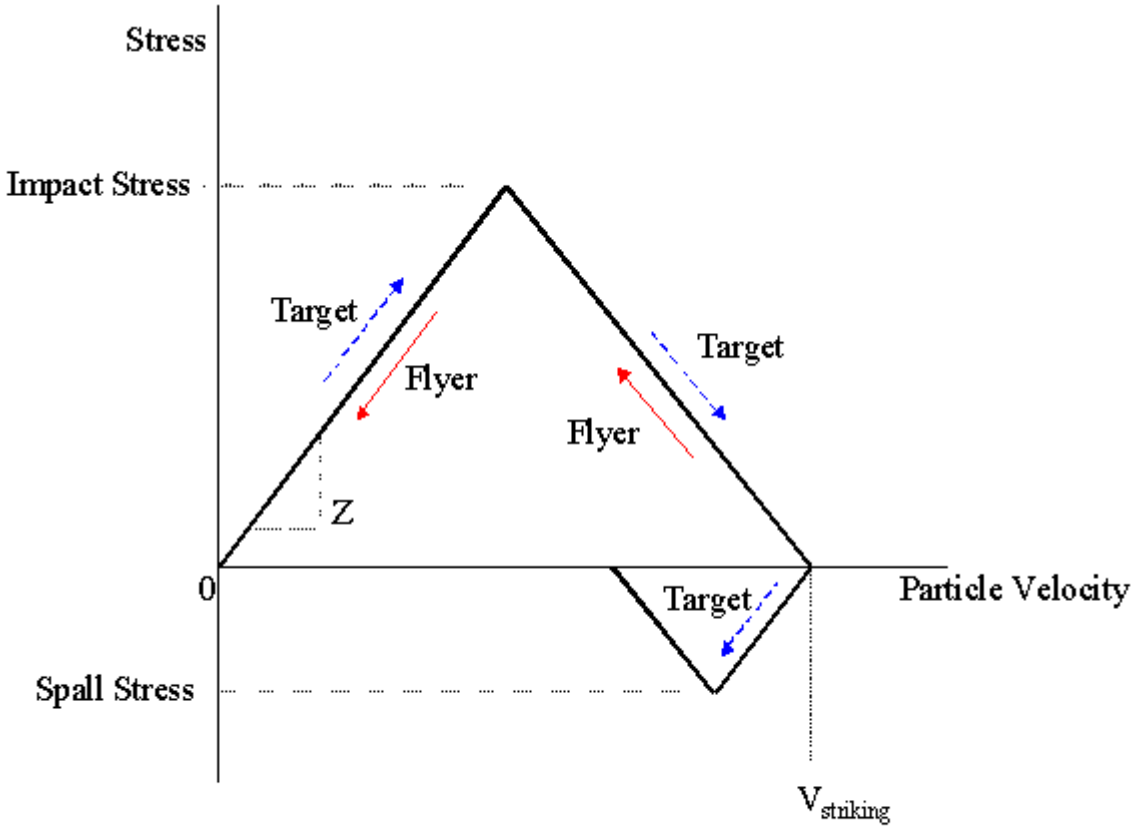

Figure 3.9: Stress vs. Particle Velocity Diagram

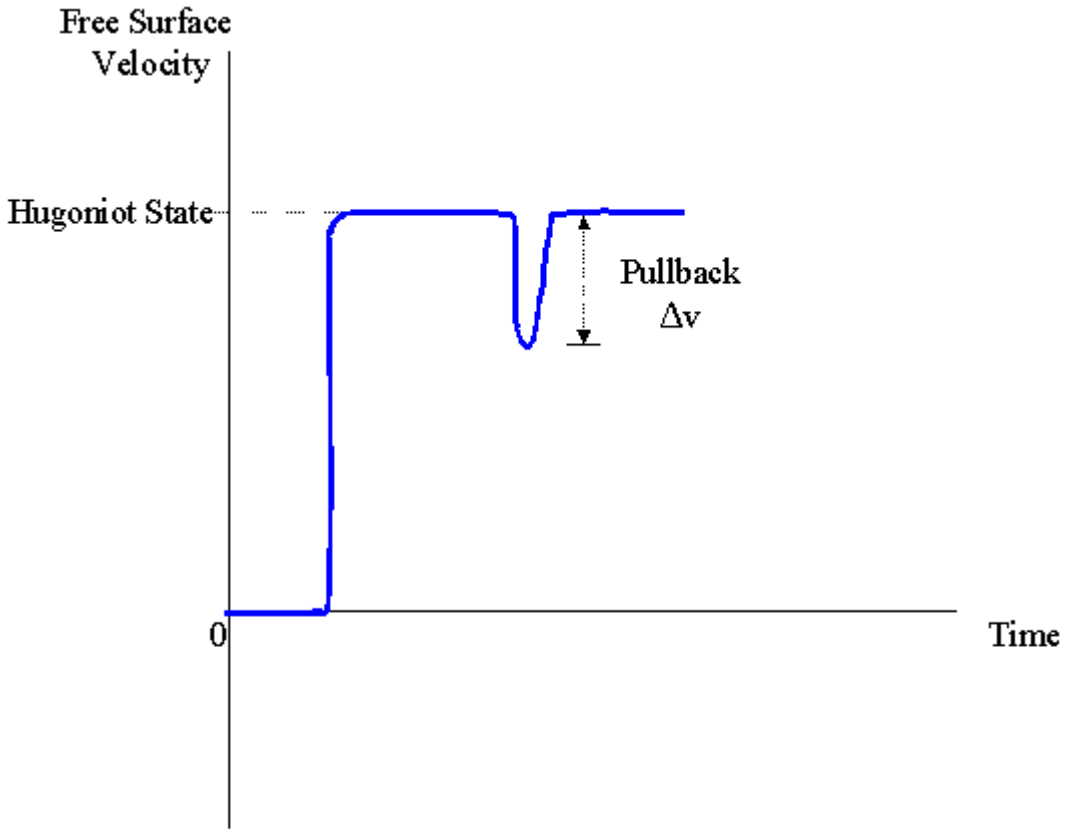

Figure 3.10: Free Surface Velocity vs. Time Diagram

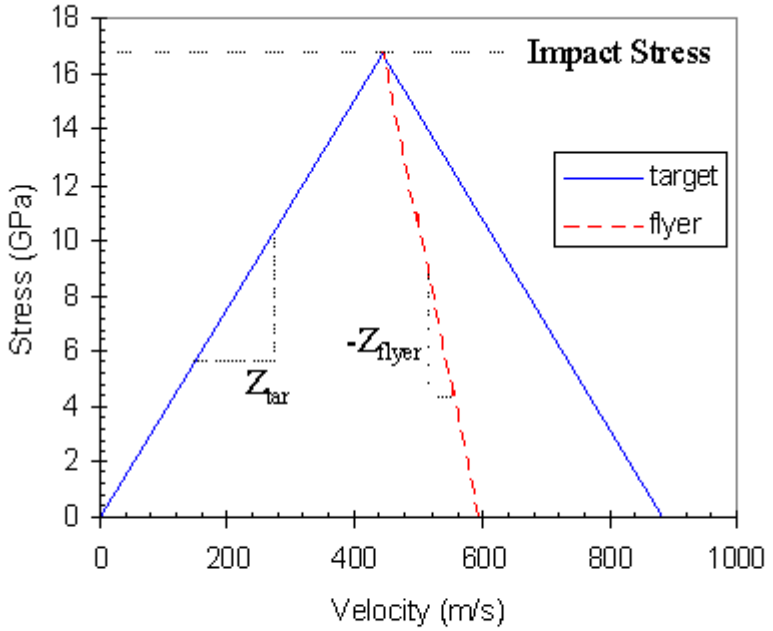

Figure 3.11: Stress vs. Velocity with Impedance Mismatch (Purely Elastic Response)

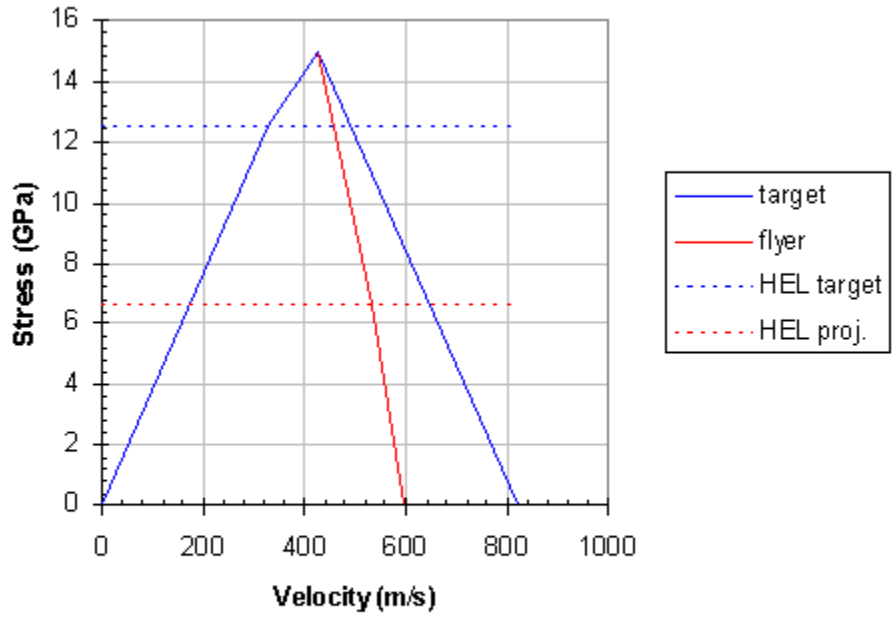

Figure 3.12: Stress vs. Velocity using Material Elastic-Plastic Response

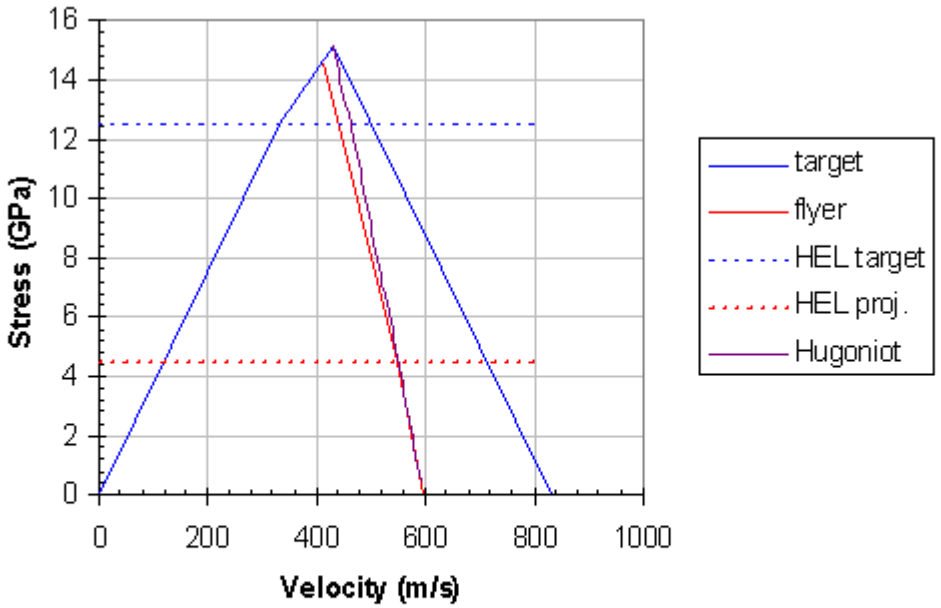

Figure 3.13: Stress vs. Velocity using Elastic-Plastic Response of Target and Hugoniot Curve of Flyer

CHAPTER 4

RESULTS

Spall Strength

Spall tests were conducted at four different velocities: 200, 300, 400 and 600 m/sec. Impact stresses were calculated to be approximately 4 GPa, 6 GPa, 8GPa, and 15 GPa, respectively. Experiments for the first three impact velocities were conducted at two different pulse widths. See Table 4.1 for a shot summary. The pulse widths were calculated using equation (3.1). For the 2mm flyers the pulse width was approximately 340ns and for the 4mm flyers it was approximately 670ns. The tests at 600 m/s were conducted using K68. The thickness of each K68 flyer created pulse widths within 36ns of the 2mm SiC pulse width. See Table 4.2 for pulse width values. The density of K68 was 14.92 g/cm^3, with c_L being 6.92 km/s, c_S being 4.16 km/sec, and c_o calculated as 4.98 km/sec (unpublished data). The bulk elastic wavespeed, c_o, was calculated using equation (2.4).

Spall strengths were plotted as a function of impact stress in Figure 4.1. The square symbols represent experiments conducted with 2mm thickness flyers, while the circles were conducted with 4mm flyers. The solid symbols represent EH while the hollow symbols represent RH. The triangular symbols represent the spall tests conducted using K68 flyers. The asterisks in the legend are simply to point out that the K68 flyers had pulse widths equivalent to 2mm of SiC.

Shots 323G, 328G, and 411H were conducted on EH at 302.9, 407.8, and 200.8 m/sec striking velocities, respectively (see Figure 4.2). For corresponding impact stress calculations see Table 4.1. The flyers were all EH with a thickness of 2mm. 411H was conducted with a 4mm target. Shot 411H had an abnormally large spall strength, which will be discussed later. Shot 408H* was conducted to determine both HEL and spall strength. The striking velocity of 601.9 m/sec was chosen to result in an impact stress above 15 GPa, well above normal values for HEL in SiC (usually 12-14 GPa). The HEL will also be discussed later in the chapter. Shots 321H, 324G, and 328H were symmetric impacts each using an EH flyer thickness of 4mm, see Figure 4.3 for results. The striking velocities for those shots were 302.9, 199.8, and 407.8 m/sec respectively. Figure 4.4 shows the effect of pulse width on the free surface velocity profiles. Spallation occurs sooner with the 2mm sample (Shot 323G) and in Figure 4.4 a wave reverberation from the newly created spall plane is apparent. The “H” and “G” in the shot designations simply refer to the VISAR used in the experiment. If two shots were conducted side by side as was discussed in Chapter 3, the shot number will be the same, however, one specimen will have used the “H” VISAR and the other will have used the “G” VISAR.

For RH, shots 323H, 325G, 327H, 403G, and 403H were symmetric impacts with 2mm thick flyers, see Figure 4.5. The impact velocities were 302.9, 203.4, 406.7, 302.6, and 302.6 m/sec respectively. Shots 403G and 403H replicated the conditions of shot 323H to test for repeatability in the spall strength measurements, see Figure 4.6. The results fell within the error bars of the original, see Figure 4.1. Shots 322H, 325H, and 327G were RH shots conducted with 4mm flyers at 302.3, 203.4, and 406.7 m/sec striking velocities, respectively (see Figure 4.7). Shot 405H* was conducted with K68 as

the flyer at a striking velocity of 593.7 m/sec. 405H* was conducted to obtain both spall and HEL.

Shot 0411H seems to be an anomaly in that all the other shots follow a similar trend, with little pulse width dependence, and little difference between the materials. The EH target in 0411H has a much higher spall strength than the similar test with the longer pulse width (324G) and than those of RH (325G and 325H). The only reasonable explanation is that the result is one of material variability. Dandekar had similar results in his study [26].

Spall strength results show similar trends to those found in Dandekar [9, 26]. Spall strengths increase up to a threshold in impact stress and then show a subsequent decline, see Figure 4.1. The threshold impact stress for both materials appears to be around 5.8 GPa. At impact stresses above the HEL the materials retain finite spall strengths. The post-HEL spall strength is lower than the other values.

For the most part, the longer pulse width experiments show slightly lower spall strengths. However, within the variability of the tests, spall strength could be considered pulse width independent. The exception could be EH at an impact stress of 8 GPa. It would be interesting to explore that the material might not become pulse width dependent until a certain threshold stress has been achieved. One possible explanation could be that the failure mechanism before the threshold impact stress is time-independent, but above it, another failure mechanism is time-dependent. If plasticity dominates over crack dynamics before the threshold and vice-versa after, then using Bourne's theory that crack dynamics are dependent on Rayleigh wave speeds could offer an explanation to the experimental data. The experiments on RH at 5.8 GPa obtained spall strength results

where the longer pulse width had a higher spall strength. However, those results are within the variability of the tests.

Experimental error was calculated using error propagation routines discussed in the book by Taylor [36]. The error associated with the VISAR measurement was used in conjunction with the errors associated with the density and longitudinal elastic wave speed measurements to determine the error bars associated with the calculated spall strength values.

HEL

As was discussed earlier, shots 405H* and 408H* were designed to determine both spall strength and HEL. The two shots were conducted with a striking velocity near 600 m/sec. There was not a clear transition from elastic to plastic rise in the free surface velocity profile. Thicker specimens were used in shots 410H** and 412H** in an attempt to exaggerate the transition. Tungsten carbide (WC) samples from Cercom were used for flyers in these experiments. The WC flyers were thicker so the experiments were conducted strictly for the purpose of determining HEL. Material data for the Cercom WC can be found in Dandekar and Grady [37]. 410H** was conducted on RH at a striking velocity of 598.6 and 412H** on EH at 607.8 m/sec. Unfortunately, the elastic-plastic transition in the latter two tests had results similar to the tests conducted with K68. See Figure 4.8 for HEL results on RH and Figure 4.9 for EH. Despite not having a clear transition, HEL values could be determined from the profiles since there was a rapidly increasing linear portion to the rise, followed by a slower sloping continuation to the Hugoniot. The HEL was taken to be this transition point. The free

surface velocity profiles were similar to those obtained by Feng and Gupta[10]; without a distinctive transition from elastic to plastic at the HEL. A possible explanation is that the plastic wave only began to form at the impact velocities tested. Higher impact stresses would allow the transition to develop. Plots with a significant transition from elastic to plastic wave rise similar to Grady's [11] require much higher impact velocities which are not achievable with the current test facilities at ARL.

At impact stresses of 15.1 GPa and 15.3 GPa, RH and EH had HEL values of 13.6 GPa and 13.9 GPa with a target thickness of 6.4 mm. At similar impact stresses with a target thickness of 9.9mm, RH and EH had HELs of 13.9 GPa and 13.1 GPa. The decreasing HEL results with increased target thickness for the EH could be described as precursor decay. However, it has been found that there is little precursor decay in ceramics. The trend in the RH HEL with thickness cannot be explained. Either it was material variability or the error associated with testing. If averages were taken of the HEL values, the HEL for RH would be 13.8 GPa and EH would be 13.5 GPa. There appears to be very little difference in HEL values between RH and EH.

Comparison to other SiCs

The threshold for the spall values occurs at slightly higher impact stresses in the Hexoloy materials, than that found for Sohio, FrS, and SiC-B. The Hexoloy thresholds occur around 5-7 GPa and the Dandekar [9] materials around 3-5 GPa. The Hexoloys appear to have spall values similar to the Sohio material, see Figure 4.10. At lower impact stresses the Hexoloys have higher spall stresses than the FrS material, at the

highest impact stress the spall strengths are similar. The HEL value for EH and RH were similar to that found by Bourne [8] for his sintered SiC.

Table 4.1: Shot Summary

Material	Shot	Flyer t	Targ. T	Impact Vel.	Impact Stress	Pullback	Spall	HEL
	#	(mm)	(mm)	(km/sec)	(GPa)	(m/sec)	(GPa)	(GPa)
Enhanced	323G	2.048	6.392	302.9	5.80	43.3	0.830	-
"	328G	2.050	6.401	407.8	7.81	34.1	0.653	-
"	411H	2.050	4.045	200.8	3.84	43.7	0.836	-
"	321H	4.044	6.398	302.9	5.80	42.2	0.807	-
"	324G	4.048	6.400	199.8	3.82	26.8	0.513	-
"	328H	4.045	6.393	407.8	7.81	28.2	0.539	-
"	408H*	1.289	6.398	601.9	15.30	14.4	0.276	13.9
"	412H**	3.999	9.854	607.0	15.30	-	-	13.1
Regular	323H	2.045	6.397	302.9	5.74	34.6	0.657	-
"	325G	2.051	6.396	203.4	3.86	32.5	0.615	-
"	327H	2.043	6.393	406.7	7.71	35.0	0.664	-
"	403G	2.050	6.402	302.6	5.74	37.6	0.712	-
"	403H	2.048	6.397	302.6	5.74	35.3	0.669	-
"	322H	4.049	6.401	302.3	5.73	37.4	0.709	-
"	325H	4.052	6.397	203.4	3.86	28.6	0.542	-
"	327G	4.049	6.398	406.7	7.71	32.5	0.616	-
"	405H*	1.288	6.396	593.7	15.10	15.2	0.288	13.6
"	410H**	4.002	9.929	598.6	15.10	-	-	13.9
	*flyer was K68							
	**flyer was WC							

Table 4.2: Pulse Widths and Times to Arrival of Cylindrical Wave

Material	Shot	Flyer t	Targ. T	Pulse Width	Arrival Cyl. Wave[1]
	#	(mm)	(mm)	(usec)	(usec)
Enhanced	323G	2.048	6.392	0.338	1.421
"	328G	2.050	6.401	0.338	1.421
"	411H	2.050	4.045	0.338	1.361
"	321H	4.044	6.398	0.667	1.421
"	324G	4.048	6.400	0.667	1.421
"	328H	4.045	6.393	0.667	1.421
"	408H*	1.289	6.398	0.373	1.421
"	412H**	3.999	9.854	1.134	1.549
Regular	323H	2.045	6.397	0.340	1.413
"	325G	2.051	6.396	0.341	1.413
"	327H	2.043	6.393	0.340	1.413
"	403G	2.050	6.402	0.341	1.413
"	403H	2.048	6.397	0.340	1.413
"	322H	4.049	6.401	0.673	1.413
"	325H	4.052	6.397	0.674	1.413
"	327G	4.049	6.398	0.673	1.413
"	405H*	1.288	6.396	0.372	1.413
"	410H**	4.002	9.929	1.135	1.548
	*flyer was K68				
	**flyer was WC				
	[1] t_4 from Figure 3.7				

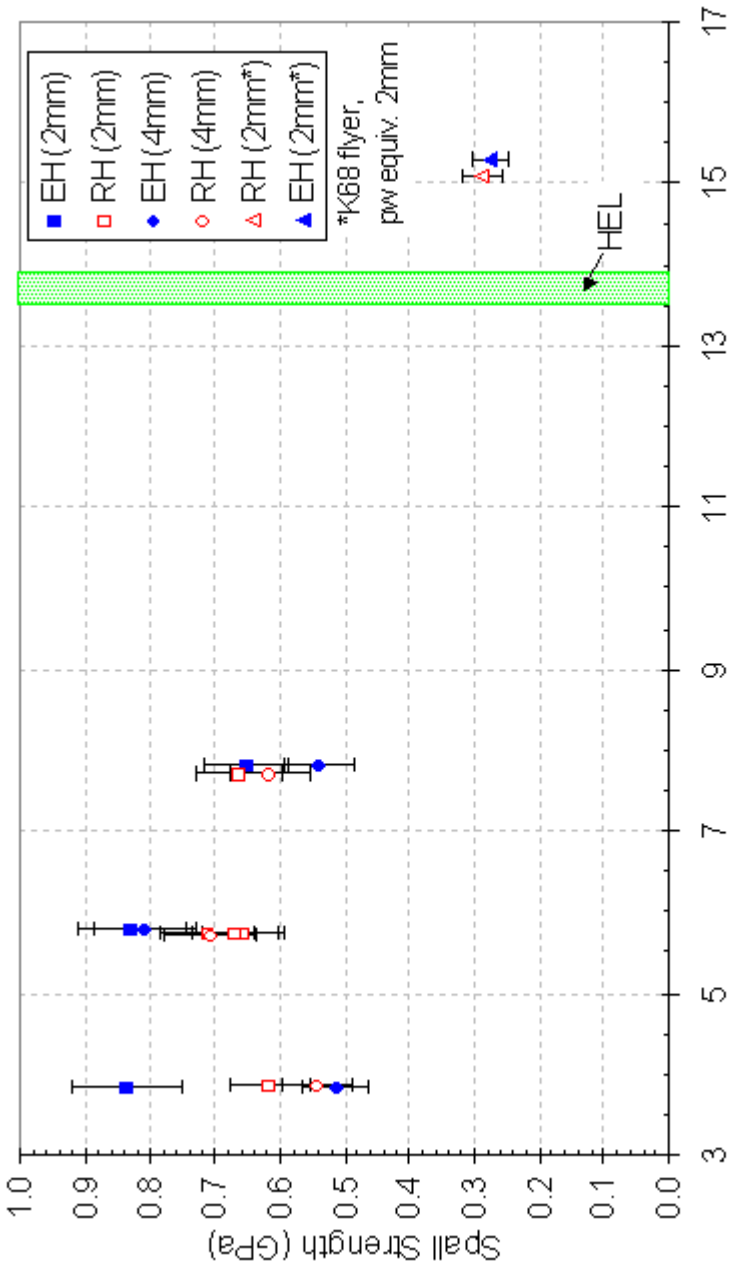

Figure 4.1: Spall Strength vs. Impact Stress

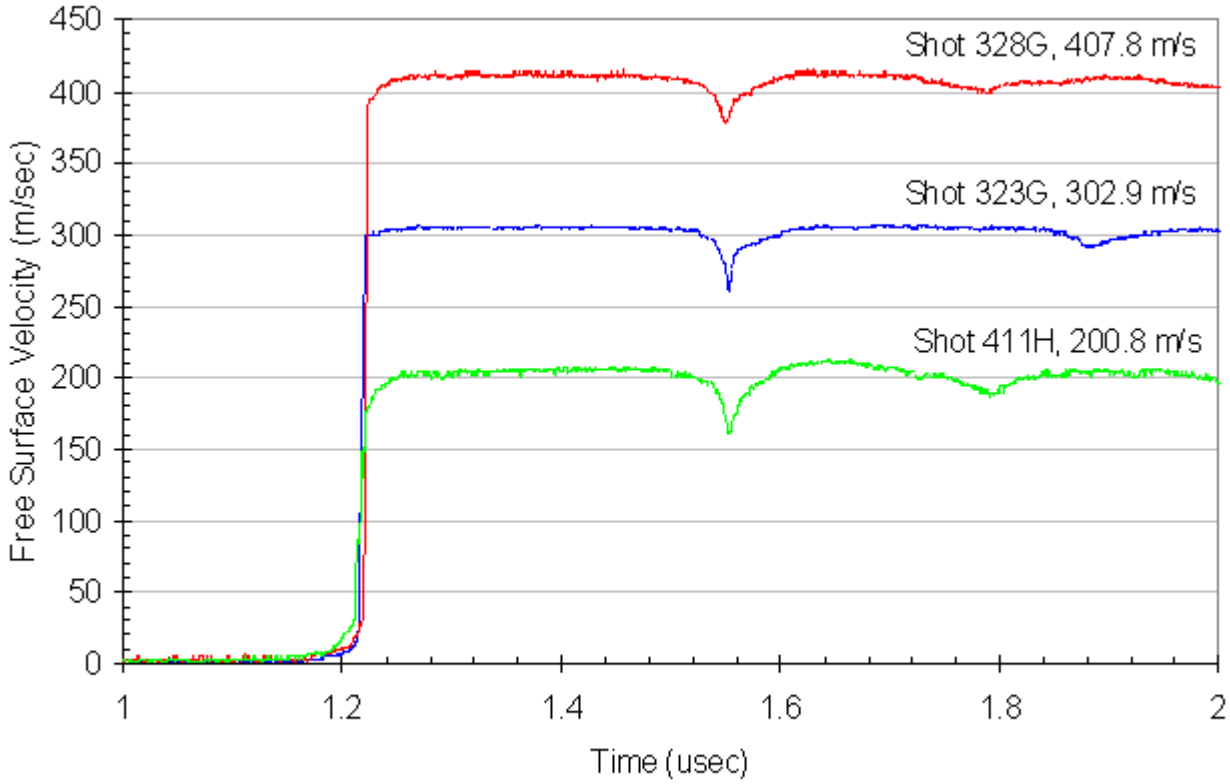

Figure 4.2: Free Surface Velocity Profiles of EH with 2mm flyers

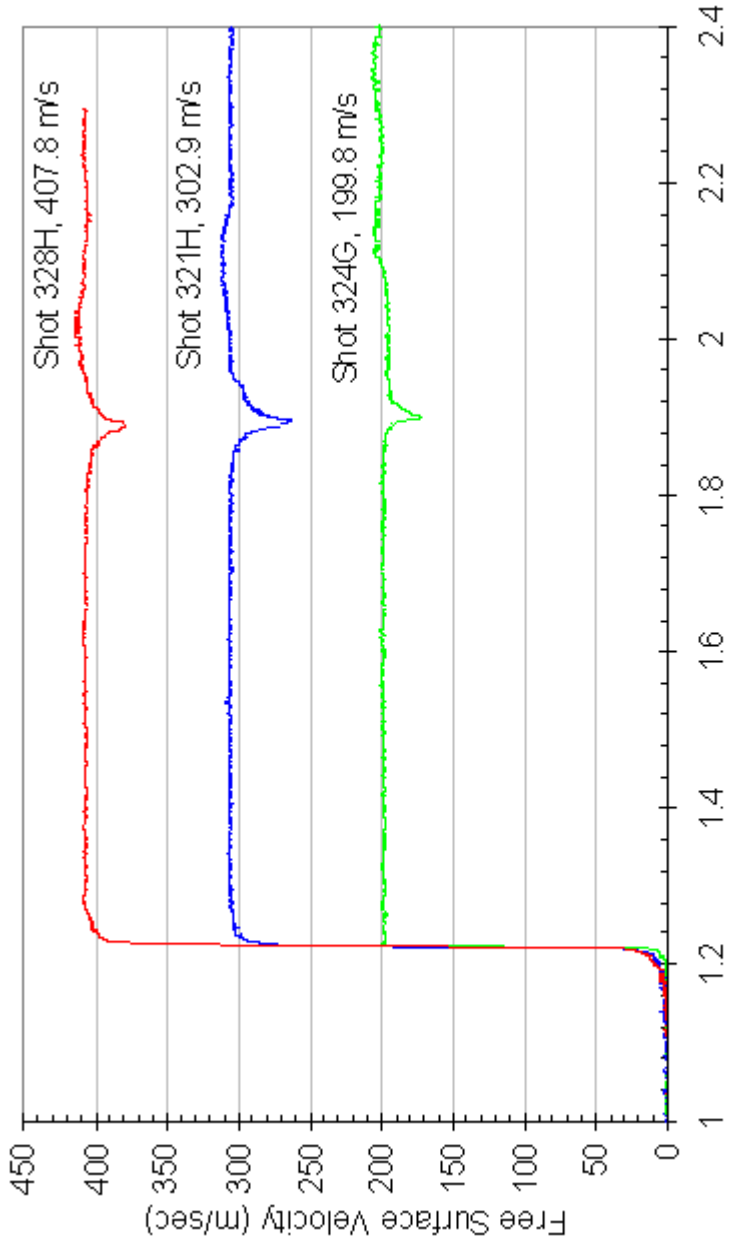

Figure 4.3: Free Surface Velocity Profiles of EH with 4mm flyers

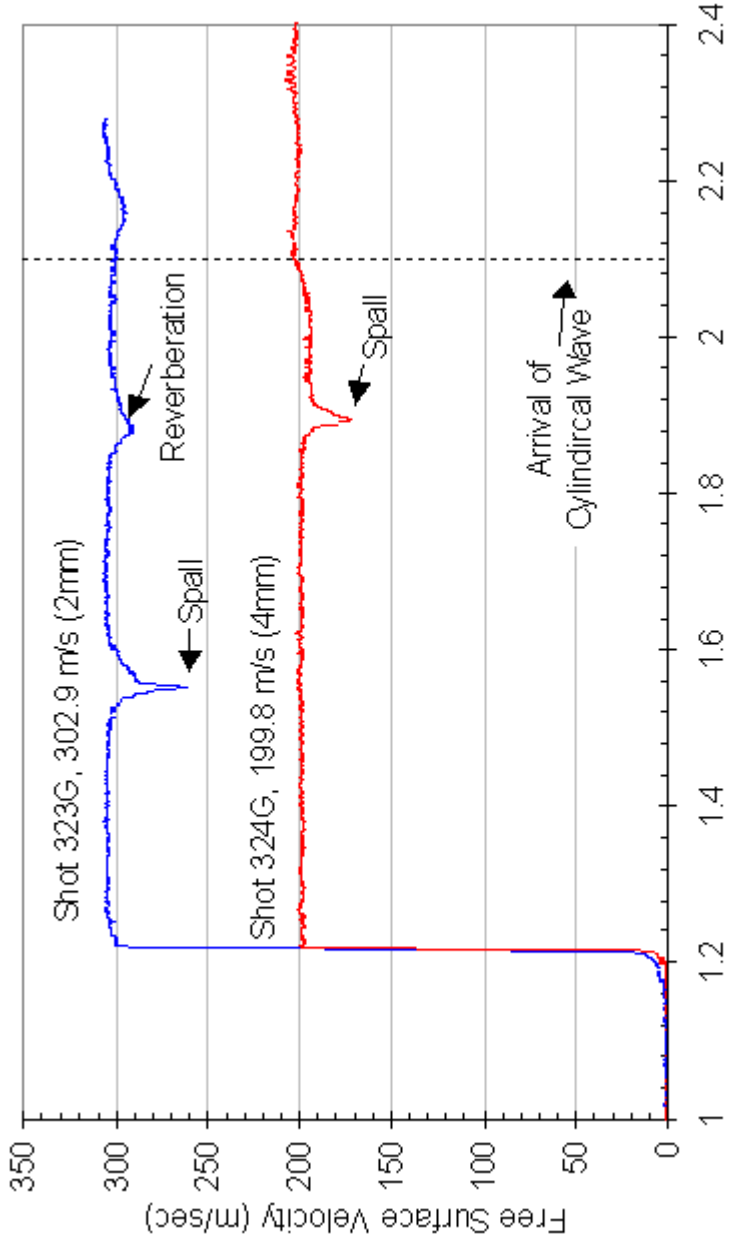

Figure 4.4: Free Surface Velocity Profiles of EH with 2mm & 4mm flyers

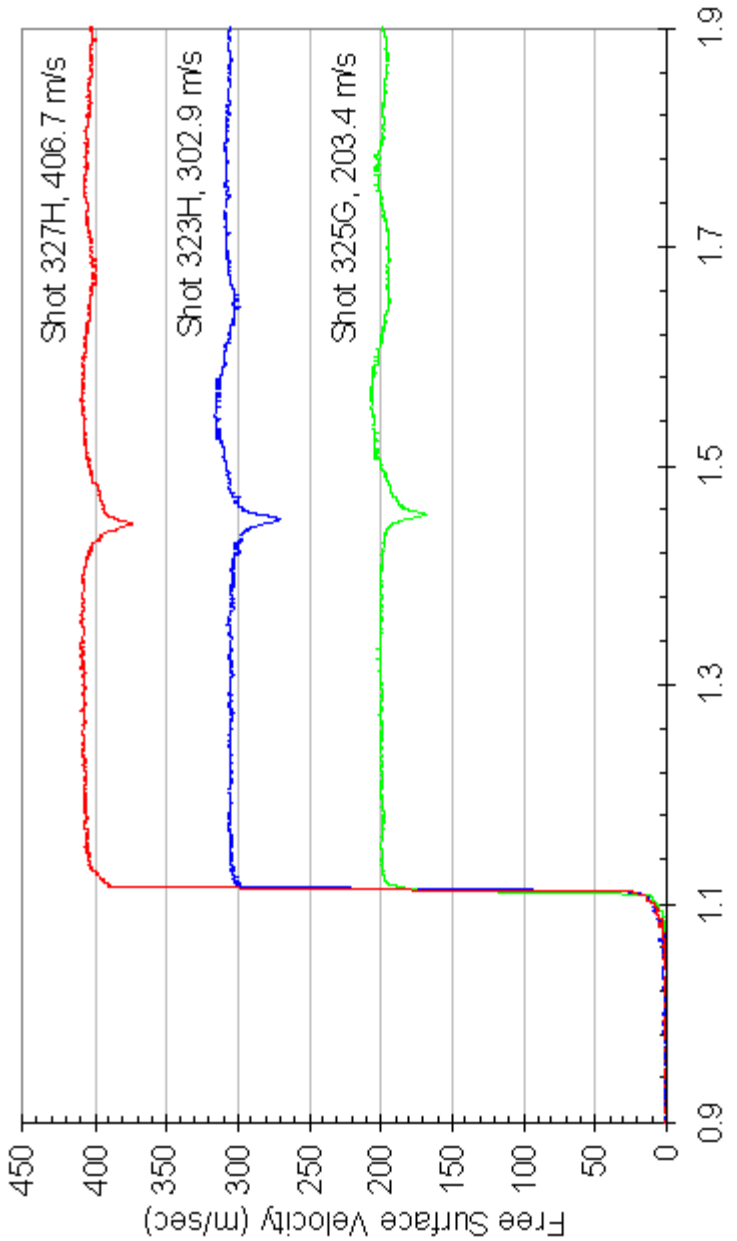

Figure 4.5: Free Surface Velocity Profiles of RH with 2mm flyers

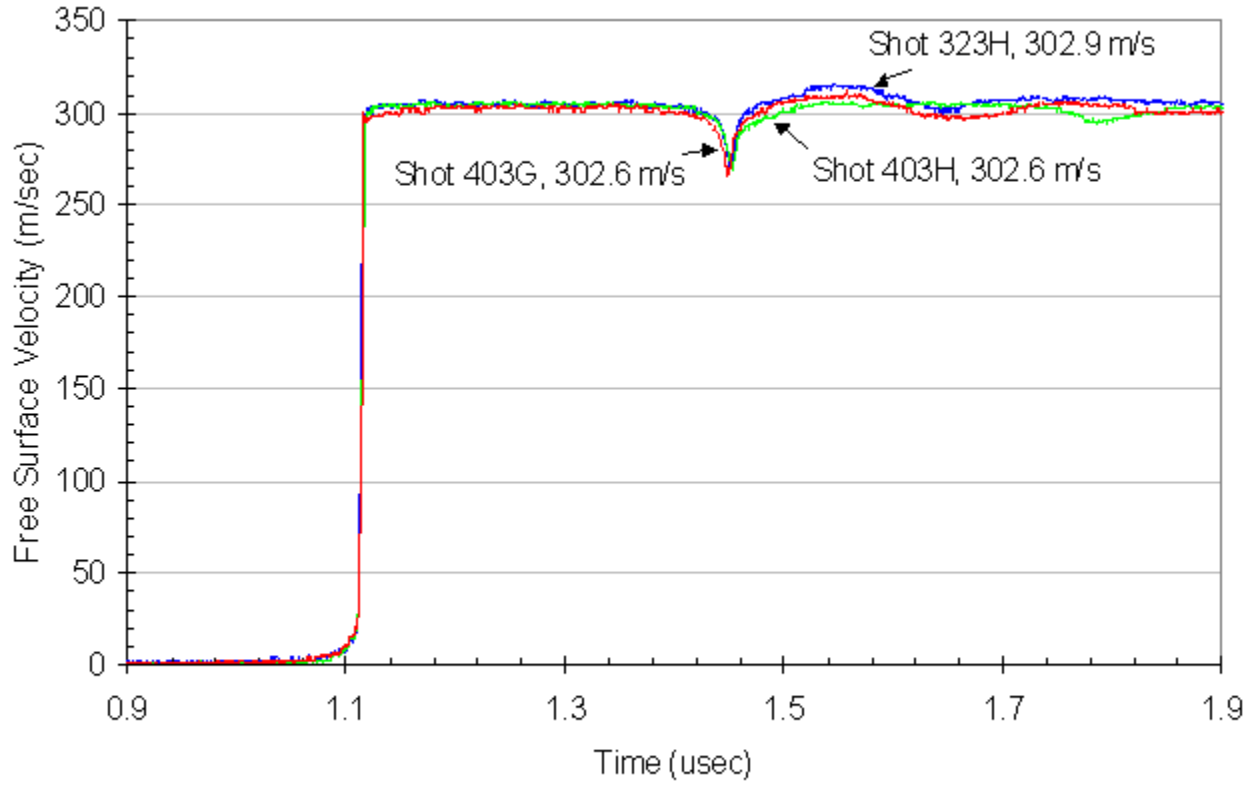

Figure 4.6: Repeatability Tests, RH at ~300m/s with 2mm Flyers

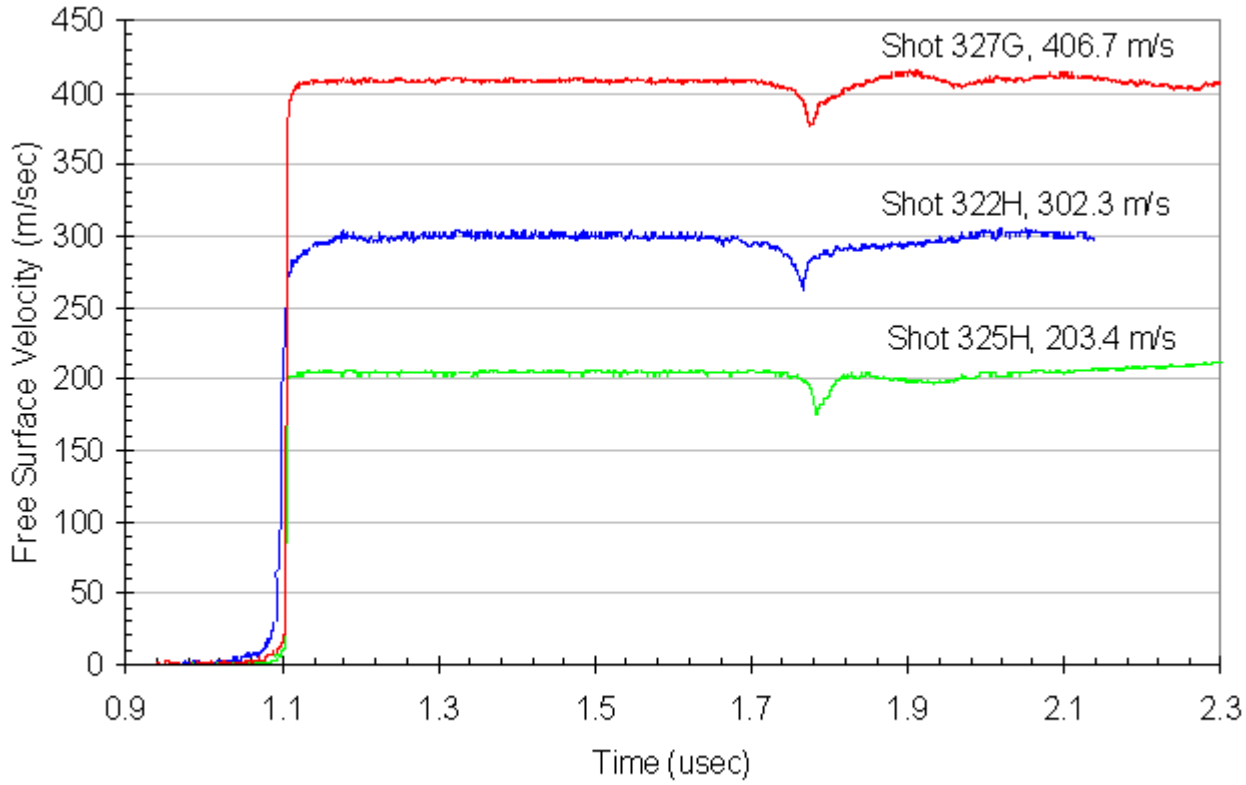

Figure 4.7: Free Surface Velocity Profiles of RH with 4mm flyers

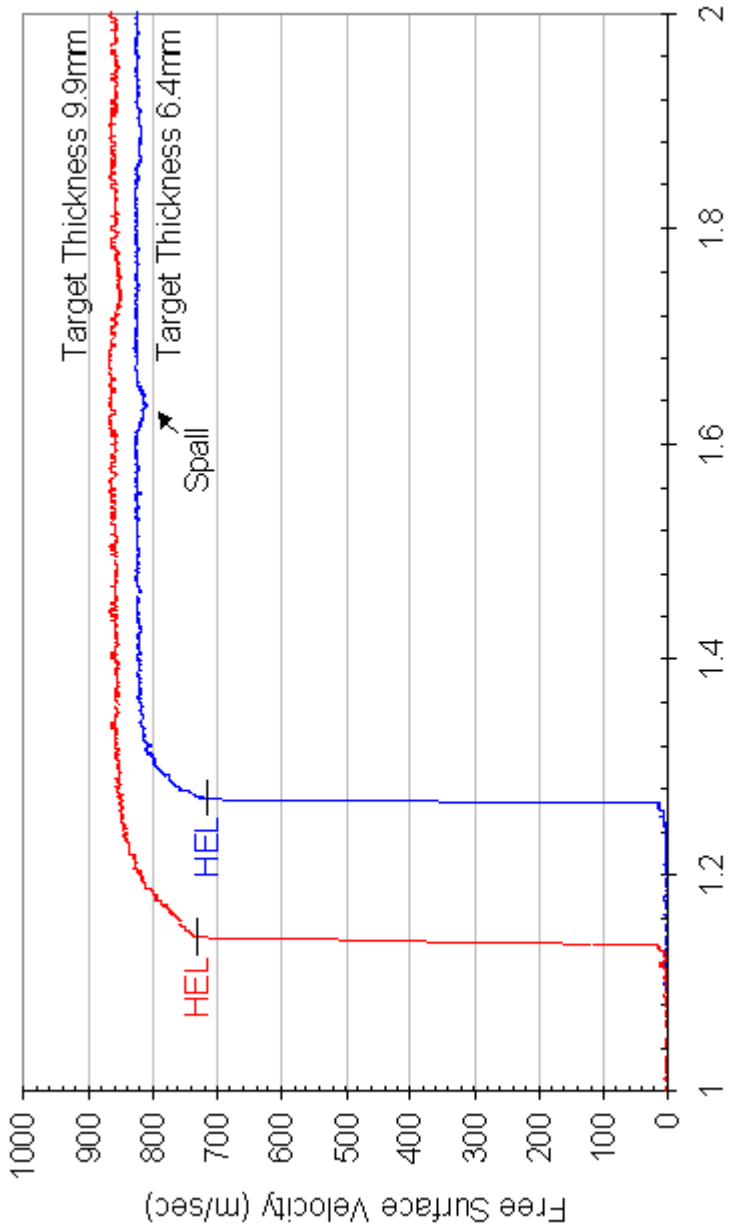

Figure 4.8: HEL Profiles for RH

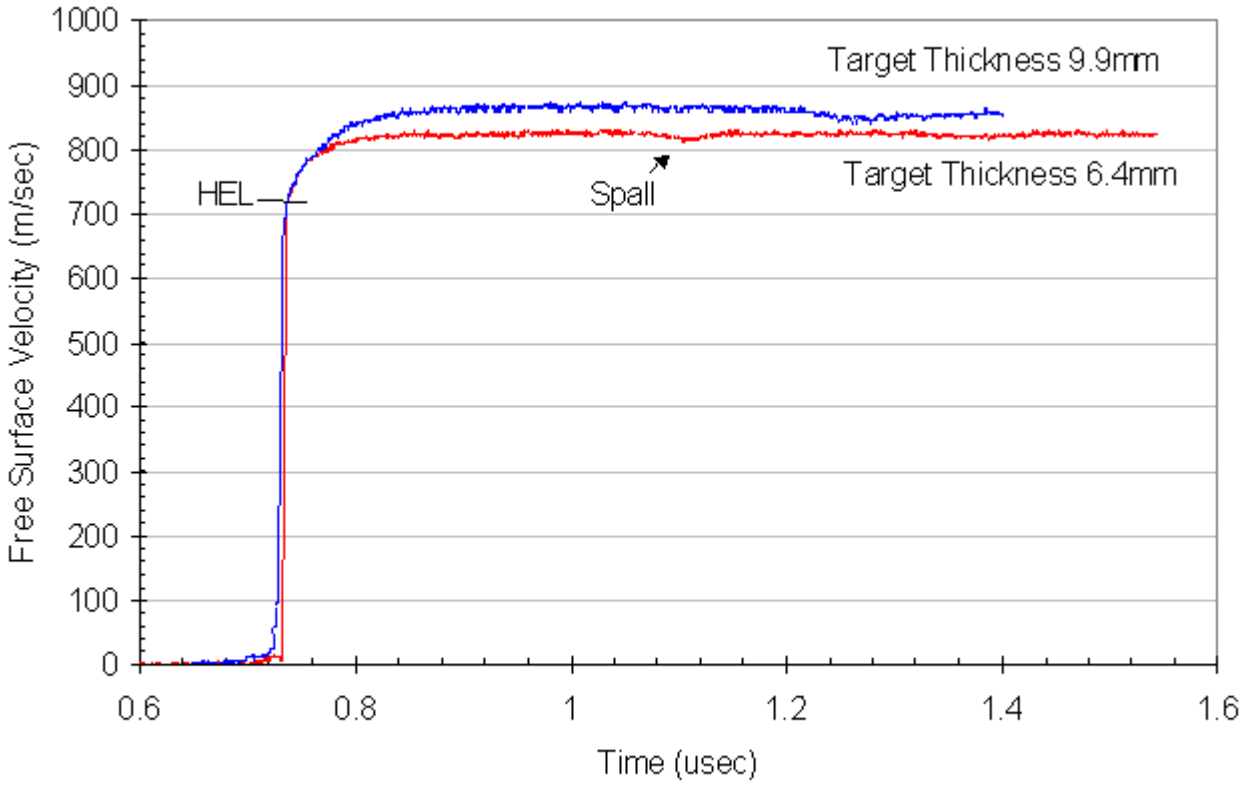

Figure 4.9: HEL Profiles for EH

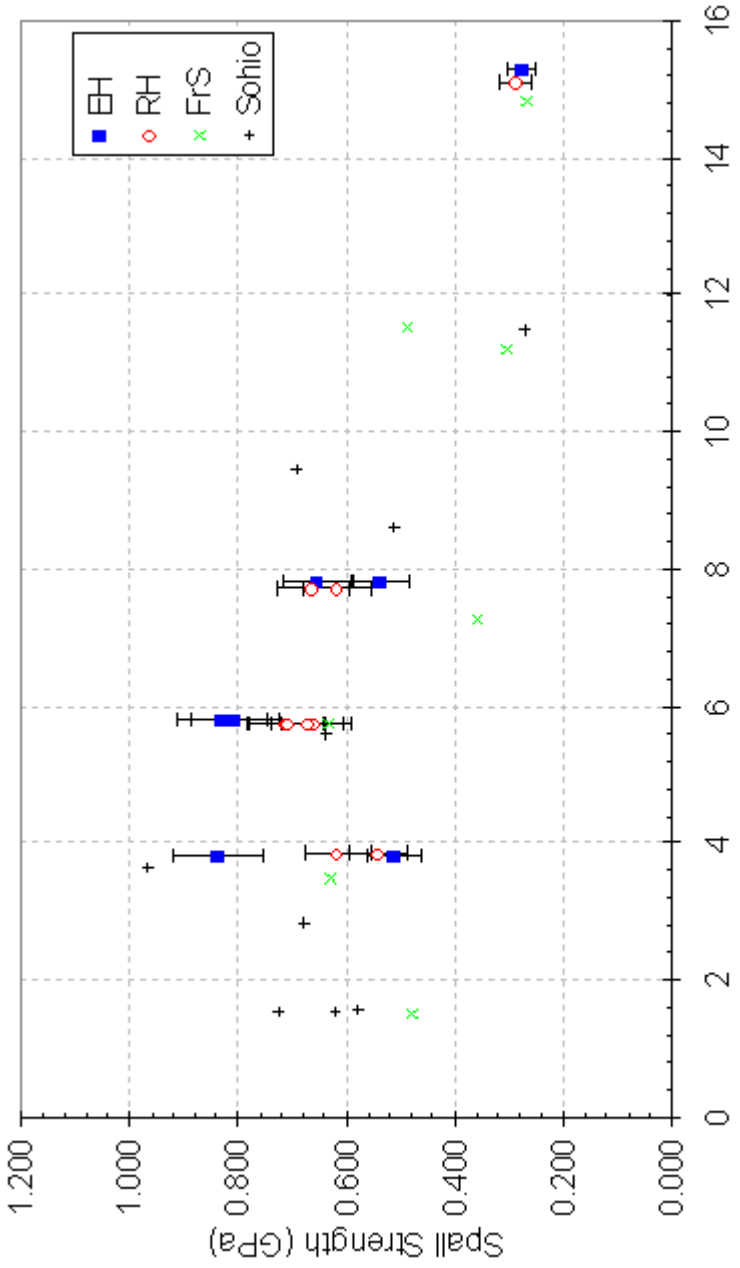

Figure 4.10: Comparison to Other SiCs

CHAPTER 5

CONCLUSIONS

Conclusions

Regular Hexoloy (RH) and Enhanced Hexoloy (EH) obtained from Saint Gobain were characterized microstructurally prior to plate impact testing. Characterization included morphology, density, elastic wave speeds, hardness, fracture toughness, and flexure strength. Results showed RH and EH to be nearly identical except for differences in porosity distribution and flexure strength. RH samples had larger and a higher number of larger sized pores. These act as large flaws and effectively lower the flexure strength of RH. EH samples had a flexure strength that was 18% higher than the RH samples. Plate impact experiments were conducted to examine the influence of porosity distributions on the HEL and spall strengths of these two materials. Spall strength experiments were conducted at different impact stresses and varying pulse widths. Stresses ranged from 3.8-15.3 GPa and pulse widths were 340ns and 670ns.

Results of these plate impact experiments showed that, within the variability of the experimental results, there was no discernable difference between the spall strength values for RH and EH within the range of impact stresses and comparable pulse widths. To test for repeatability of the spall strength results, one impact condition was repeated. The three experiments on RH at an impact stress of 5.8 GPa, with a pulse width of 340ns show spall strength results within 8 percent of each other. The spall strengths showed a similar trend as observed by Dandekar and Bartkowski [9, 25, 26] with respect to impact

stress. In SiC, spall strengths increase with impact stress to a threshold value and then decline. The threshold value for RH and EH appears to be between 5-7 GPa. Both materials show finite spall strengths above the respective HEL. The HEL values for RH samples and EH samples were 13.8±0.2 GPa and 13.5±0.6 GPa, respectively.

Despite the effect the large pores had on the quasi-static flexure strength levels between RH and EH, they had little influence on the dynamic behaviors. The triaxial stresses associated with uniaxial strain conditions seen in the plate impact tests did not allow the bigger pores in RH to effect spall strength or HEL. The triaxial stress state confines the formation of large cracks from larger pores. Without the release in stress from the large cracks, a greater number of smaller pores and flaws affect material dynamic behavior. In contrast, the uniaxial stress conditions imposed by the four-point bend strength tests allow the initiation and propagation of large cracks from the large pores in RH.

In addition to the triaxial stress state, another possible reason for lack of difference between the spall strength values between RH and EH could be the result of the compressive wave that passes through the target prior to spallation. The damage caused by the compressive loading could be more severe than the damage caused by the large pores. This would result in similar spall strength values between the two material varieties.

The spall strength results of the Hexoloys were comparable to the other sintered materials tested by Dandekar [9, 25, 26] and had lower spall strengths than the hot pressed varieties. The HEL of the Hexoloys was comparable to that measured by Bourne [8] for his sintered SiC.

Future Work

It would be beneficial to do the same shock-reshock work that Dandekar performed on TiB_2 [29]. This could determine if there are different mechanisms of fracture leading to the increase then subsequent decrease in spall strength as a function of impact stress in silicon carbides.

It would also be useful to perform plate impact experiments on the SiC samples made by Moberlychan, et al. [33] with a reported fracture toughness of around 9 MPa. This material is hot pressed and could be compared to the results of SiC-B, which only has a fracture toughness of around 5 MPa (company data). A material with a higher fracture toughness should be able to better resist damage during the compressive portion of a spall test and in effect have a higher spall strength when experiencing the subsequent tensile stresses. Similarly, except in a reverse manner, it would be interesting to look at the fracture toughness values of the FrS and FS&HP materials tested by Dandekar [9, 25, 26]. The only difference between the FS&HP and the FrS variety is an extra HIPing step, which leads to a significant increase in spall values.

It would also be beneficial to conduct recovery experiments much like those performed on alumina [12, 17]. Pre- and post-impact microstructural analysis of specimens would offer insight into the failure mechanisms at different impact regimes. Unfortunately, at higher velocities recovery experiments are difficult as usually the aftermath is merely dust. Ideally, recovery experiment samples with extensive large-scale macrocracks are desired. It is a catch-22 situation, one would like to analyze the

failure mechanisms associated with higher impact stresses, but the higher impact stresses make it harder to recover the specimen.

APPENDIX

SPECIMEN PREPARATION

Sectioning

Make sure sample is square and securely held in diamond saw. For SiC use a diamond blade speed of 2500 rpm and a federate of 0.5 in./min.

Polishing

First set samples in bakelite. Then follow the below process in Table A.1 for polishing SiC using the automated polisher.

Table A.1: Polishing Procedure for SiC

Force (N)	Time (min.)	Size Abbrasive (microns)	Abbrasive Type	Wheel/Holder Spin	Wheel speed
15	3	45	Diamond film	Opposite	150 rpm
15	3	30	Diamond film	Opposite	150 rpm
30	4	15	Diamond slurry	Opposite	150 rpm
30	4	6	Diamond slurry	Opposite	150 rpm
30	8	1	Diamond slurry	Opposite	150 rpm
30	8	Colloidal Silica	Diamond slurry	Opposite	150 rpm

Etching

Polished samples must be taken out of bakelite before etching. Use a modified-murakami solution to etch the SiC samples.

Ingredients:

20g NaOH

20g $K_3Fe(CN)_6$

50mL H_20

Setup a stand in a hood and wearing the appropriate safety equipment, weigh and then mix the ingredients together in a pyrex beaker. Boil for approximately 10 minutes.

Lapping and Polishing (ARL)

The 9.9 mm plate impact specimens were prepared at ARL. Precut cylindrical specimens were lapped on a Lapmaster lapping machine using 500 grit SiC particles. Once the faces of the specimen were lapped flat, the probe side was manually polished on a polishing wheel. The process is described in Table A.2.

Table A.2: Preparation of Plate Impact Specimens

Abbrasive Size (microns)	Abbrasive Type	Polishing Cloth	Approx. Time
~26 (500 grit)	SiC particles	--	--
15	Diamond slurry	Texmet P	5min
3	Diamond slurry	Texmet P	5min
1	Diamond slurry	Texmet2000	5min

REFERENCES

1. Hauver, G.E., et al. *Enhanced ballistic performance of ceramic targets.* in *Proceedings of the 19th Army Science Conference, USA*. 1994.
2. Lundberg, P., R. Renstrom, and B. Lundberg, *Impact of metallic projectiles on ceramic targets: transition between interface defeat and penetration.* International Journal of Impact Engineering, 2000. **24**: p. 259-275.
3. Grady, D.E., *Shock-wave compression of brittle solids.* Mechanics of Materials, 1998. **29**: p. 181-203.
4. Grady, D.E., *Shock-wave strength properties of boron carbide and silicon carbide.* Journal de Physique IV, 1994. **4**(Septembre 1994): p. C8-385 to C8-391.
5. Orphal, D.L. and R.R. Franzen, *Penetration of Confined Silicon Carbide Targets by Tungsten Long Rods from 1.5 to 4.6 km/s.* International Journal of Impact Engineering, 1997. **19**(1): p. 1-13.
6. Orphal, D.L., et al., *Penetration of Confined Boron Carbide Targets by Tungsten Long Rods at Impact Velocities from 1.5 to 5.0 km/s.* International Journal of Impact Engineering, 1997. **19**(1): p. 15-29.
7. Orphal, D.L., et al., *Penetration of Confined Aluminum Nitride Targets by Tungsten Long Rods at 1.5-4.5 km/s.* International Journal of Impact Engineering, 1996. **18**(4): p. 355-368.
8. Bourne, N., J. Millett, and I. Pickup, *Delayed failure in shocked silicon carbide.* Journal of Applied Physics, 1997. **81**(9): p. 6019-6023.
9. Dandekar, D.P. and P. Bartkowski, *Spall strengths of silcon carbides under shock loading*, in *Fundamental Issues and Applications of Shock-Wave and High Strain-Rate Phenomena*, K.P. Staudhammer, L.E. Murr, and M.A. Meyers, Editors. 2001, Elsevier Science Ltd. p. 71-77.
10. Feng, R., G.F. Raiser, and Y.M. Gupta, *Material strength and inelastic deformation of silicon carbide under shock wave compression.* Journal of Applied Physics, 1998. **83**(1): p. 79-86.
11. Grady, D.E., *Shock Profile Studies on Selected Silicon Carbide Ceramics with Application to Dynamic Yield Mechanisms.* Shock Compression of Condensed Matter-1999, 2000: p. 629-632.
12. Raiser, G.F., *Dynamic Failure Resistance of Ceramics and Glasses*, in *Engineering*. 1993, PhD Thesis Brown University. p. 180.
13. Bourne, N., et al., *The effect of microstructural variations upon the dynamic compressice and tensile strengths of aluminas.* Proc. R. Soc. Lond. A, 1994(446): p. 309-318.
14. Longy, F. and J. Cagnoux, *Plasticity and Microcracking in Shock-Loaded Alumina.* Journal of the American Ceramic Society, 1989. **72**(6): p. 971-979.
15. Lee, W.E. and M.W. Rainforth, *Ceramic Microstructures: Property Control By Processing*. 1994, London, U.K.: Chapman & Hall.
16. Grady, D.E. *Shock-Wave Properties of High-Strength Ceramics*. in *Shock Compression of Condensed Matter-1991*. 1991: Elsevier Science.

17. Longy, F. and J. Cagnoux. *Plate-Impact Recovery Experiments of Ceramics*. in *Shock Compression of Condensed Matter - 1989*. 1989. Albuquerque, New Mexico: Elsevier Science Publishers.
18. Kumar, P. and R.J. Clifton, *A star-shaped flyer for plate-impact recovery experiments.* Journal of Applied Physics, 1977. **48**: p. 4850.
19. Cagnoux, J. *Spherical Waves in Pure Alumina, Effects of Grains Size on Flow and Fracture*. in *Shock Compression of Condensed Matter - 1989*. 1989. Albuquerque, New Mexico: Elsevier Science Publishers.
20. Brar, N.S., Z. Rosenberg, and S.J. Bless. *Applying Steinberg's Model to the Hugoniot Elastic Limit of Porous Boron Carbide Specimens*. in *Shock Compression of Condensed Matter 1991*. 1991. Williamsburg: Elsevier Science.
21. Dandekar, D.P. and P. Bartkowski. *Shock Response of AD995 Alumina*. in *The AIP Conference Proceedings 309 Part 1*. 1994.
22. Kennedy, G., et al., *Dynamic high-strain-rate mechanical behavior of microstructurally biased two-phase $TiB_2 + Al_20_3$ ceramics.* Journal of Applied Physics, 2002. **91**(4): p. 1921-1927.
23. Gust, W.H., A.C. Holt, and E.B. Royce, *Dynamic yield, compressional, and elastic parameters for several lightweight intermetallic compounds.* Journal of Applied Physics, 1973. **44**(2): p. 550-560.
24. Grady, D.E. and M.E. Kipp, *Shock Compression Properties of Silicon Carbide*. 1993, Sandia National Laboratory.
25. Bartkowski, P. and D.P. Dandekar. *Spall Strengths of Sintered and Hot Pressed Silicon Carbide*. in *Shock Compression of Condensed Matter-1995*. 1996: American Institute of Physics.
26. Dandekar, D.P. and P. Bartkowski, *Tensile Strengths of Silicon Carbide (SiC) Under Shock Loading*. 2001, Army Research Laboratory. p. 38.
27. Beylat, L. and C.E. Cottenot. *Post-Mortem Microstructural Characterization of SiC Materials After Interaction With a Kinetic Energy Projectile*. in *Structures Under Shock and Impact IV*. 1996: Computational Mechanics Publications.
28. Winkler, W.-D. and A.J. Stilp. *Spallation Behavior of TiB2, SiC, and B4C Under Planar Impact Tensile Stresses*. in *Shock Compression of Condensed Matter-1991*. 1991: Elsevier Science.
29. Dandekar, D.P. and D.C. Benfanti, *Strength of titanium diboride under shock wave loading.* Journal of Applied Physics, 1993. **73**(2): p. 673-679.
30. Prochazka, S., *Sintering of Silicon Carbide.* General Electric Report, 1973. **73**: p. CRD 325.
31. Lee, W.E. and M.W. Rainforth, *Chapter 7: Synthetic structural non-oxides*, in *Ceramic Microstructures Property Control By Processing*. 1994, Chapman & Hall: London, U.K. p. 415-432.
32. Achenbach, J.D., *Wave Propagation in Elastic Solids*. 1975: Elsevier Science Publishers.
33. Moberlychan, W.J., J.J. Cao, and L.C. De Jonghe, *The Roles of Amorphous Grain Boundaries and the beta-alpa Transformation in Toughening SiC.* Acta Materialia, 1998. **46**(5): p. 1625-1635.

34. Quinn, G.D. and J.A. Salem, *Effect of Lateral Cracks on Fracture Toughness Determined by the Surface-Crack-in-Flexure Method.* Journal of the American Ceramic Society, 2002. **85**(4): p. 873-879.
35. Barker, L.M. and R.E. Hollenbach, *Laser interferometer for measuring high velocities of any reflecting surface.* Journal of Applied Physics, 1972. **43**(11): p. 4669-4675.
36. Taylor, J.R., *An Introduction to Error Analysis*. Second ed. 1996: Univeristy Science Books.
37. Dandekar, D.P. and D.E. Grady. *Shock Equation of State and Dynamic Strength of Tungsten Carbide*. in *Shock Compression of Condensed matter-2001*. 2002: American Institute of Physics.